Journal of Hydrology: Regional Studies 65 (2026) 103431

Contents lists available at ScienceDirect

Journal of Hydrology: Regional Studies

journal homepage: www.elsevier.com/locate/ejrh

Zero-flow and hydrotype estimation with karst-SWAT and Sentinel-2 data in the Keritis Basin, Crete

G. Manfreda [a,*], C. Cavallo [b], M.A. Lilli [c], A. Maragkaki [c], G. Negro [a], M.N. Papa [b], N. P. Nikolaidis [c], P. Vezza [a,d]

[a] Department of Environment, Land and Infrastructure Engineering, Polytechnic University of Torino, Torino 10129, Italy
[b] Department of Civil Engineering, University of Salerno, Fisciano, SA 84084, Italy
[c] School of Chemical and Environmental Engineering, Technical University of Crete, Polytechneioupolis, Chania, Greece
[d] INGENIO CSIC-UPV, Universitat Politècnica de València, València, Spain

ARTICLE INFO

Keywords:
Non-perennial rivers
Zero-flow events
Hydrological model
SWAT
Satellite images
Sentinel-2

ABSTRACT

Study region: The Keritis Basin is located on the Island of Crete (Greece).
Study focus: This study presents a novel methodology integrating satellite imagery and hydrological modeling to provide daily forecasts of flow conditions in two non-perennial reaches of the Keritis River (Greece) during 2019–2023. A Karst-SWAT model was used to estimate daily streamflow and classified Sentinel-2 images were used to derive flow condition (flowing, ponding or dry). The combined dataset enabled the definition of critical thresholds to distinguish transitions from flowing to zero-flow events and between ponding and dry conditions.
New hydrological insights for the region: The integrated approach significantly improved the understanding of flow intermittency patterns at the daily scale by quantifying zero-flow events and estimating the hydrotype of the river reaches. Both studied reaches of the Keritis River were classified as Intermittent–Fluent. However, they exhibited pronounced interannual variability, largely driven by hydrological droughts. Water balance analysis indicates that deep aquifer recharge, due to the complex karst system, plays a primary role in controlling the occurrence of annual drying events, while evapotranspiration primarily modulates the frequency and magnitude of zero-flow peaks.

1. Introduction

Non-Perennial Rivers (NPRs) are watercourses where the surface flow ceases temporarily both in time and space (Datry et al., 2018). The latest research estimated that NPRs are prevalent in the global river network (Datry et al., 2023a; Messager et al., 2021), confirming their presence in arid and semi-arid regions as well as temperate, humid tropical, boreal, and arctic areas (Costigan et al., 2017). Climate change and anthropogenic pressures, such as water abstractions or land use changes, enhance the global shift from perennial to non-perennial regimes in the river network (Döll and Schmied, 2012). These fluvial environments are characterized by the occurrence of three different Flow Conditions (FCs): (i) Flowing "F", the surface flow is continuous; (ii) Ponding "P", there is no continuity of surface flow along the reach and water remains, usually, in isolated ponds or pools; and (iii) Dry "D", when the riverbed is completely dry (Gallart et al., 2017; Magand et al., 2020). NPRs provide fundamental ecosystem services, playing a crucial role in

* Corresponding author.
E-mail address: giammarco.manfreda@polito.it (G. Manfreda).

https://doi.org/10.1016/j.ejrh.2026.103431
Received 30 September 2025; Received in revised form 9 March 2026; Accepted 6 April 2026
Available online 10 April 2026
2214-5818/

aquifer regulation, in preserving biodiversity and biogeochemical integrity, and supplying nutrients and food (Acuña et al., 2014; Datry et al., 2018; Magand et al., 2020). Especially in arid and semi-arid regions, dry riverbeds represent a crucial environment for terrestrial species (Steward et al., 2012; Vidal-Abarca Gutiérrez et al., 2023), while isolated ponds play a vital role in supporting the resilience and recolonization of the aquatic ecosystem (Bonada et al., 2020).

The European Water Framework Directive (WFD, EU 2000) establishes that each member state must identify, categorize water bodies, and define distinct river hydrotypes and their reference condition to enable an accurate assessment of their ecological status (Heiskanen et al., 2004; Van de Bund, 2009). However, managing and identifying NPRs presents significant challenges for water authorities, as no standardized classification system exists specifically for management purposes, despite the burgeoning literature on intermittent rivers proposing various classification frameworks (Gallart et al., 2017; Munné et al., 2021).

The difficulty comes from the historical marginalization of NPRs, largely due to the limited cultural and social awareness about their relevance (Llanos-Paez and Acuña, 2022), leading to a focus of the academic community and river managers on perennial rivers rather than NPRs (Allen et al., 2020; Cottet et al., 2023). Devaluing their ecological role, NPR reaches are rarely equipped with streamflow stations (Krabbenhoft et al., 2022; Messager et al., 2021), determining a lack of information about the frequency and extent of intermittent events. Moreover, traditional gauging stations demonstrated unsuitability in catching the high spatial variability of zero-flow events, both laterally and longitudinally (Cavallo et al., 2022; Krabbenhoft et al., 2022; Zimmer et al., 2020).

Streamflow intermittence is influenced by natural processes and anthropogenic factors, occurring across different spatial and temporal scales (Costigan et al., 2016; Gómez-Gener et al., 2021). Climatic conditions, such as precipitation, temperature, and evapotranspiration, play a crucial role (Botter et al., 2021; McDonough et al., 2011). Geomorphological characteristics, such as river planform, topography, and landscape structure, also shape their behavior (Prancevic and Kirchner, 2019; Snelder et al., 2013). Additionally, subsurface properties like lithology, soil composition, and water table levels are fundamental drivers for the alternation of different FCs (Abhervé et al., 2024; Carlier et al., 2018; Costigan et al., 2017). Moreover, anthropogenic activities, including land use changes and water management practices, further alter flow dynamics (Datry et al., 2023b).

Hydrological models, especially rainfall-runoff models, are a common instrument for predicting streamflow time series and their alterations in river basins (Devia et al., 2015), but their application to NPRs is limited. Major limitations include a general tendency to overestimate the discharge during low-flow conditions and zero-flow events, potentially leading to inaccurate assessments of NPRs (De Girolamo et al., 2015; Kirkby et al., 2011). Furthermore, hydrological models commonly require a large amount of locally recorded data to be properly calibrated for representing the complexity of the process at a basin scale. Especially for streams with rapid hydrological responses, such as small streams in the Mediterranean-climate region, at least 20 years of daily data are necessary (De Girolamo et al., 2017; Zimmermann et al., 2014). The Soil and Water Assessment Tool (SWAT, Arnold et al., 1998) demonstrates good results in modeling long series of streamflow in NPRs (Jaeger et al., 2014; Levick et al., 2018; Llanos-Paez et al., 2023), providing consistent results even using only one year of hydrological and climatic observations (De Girolamo et al., 2022). Although the SWAT model is one of the most used hydrological models worldwide in different contexts (Francesconi et al., 2016; Krysanova and White, 2015), it is still challenging to simulate correctly the flow pattern between river and groundwater, especially in landscapes where complex topography and geology are present (Dohman et al., 2021; Sánchez-Gómez et al., 2024). These criticisms are particularly pronounced in karst regions, where karst features (i.e., epikarst, matrix, conduit, or springs) significantly affect the hydrological response of the catchment area (Eini et al., 2020). Researchers have addressed these challenges by combining SWAT with karst-specific models to simulate both surface flow and karst spring flow separately (Nerantzaki et al., 2020; Nikolaidis et al., 2013). However, studies focusing on karst areas remain scarce (Ricci et al., 2023).

To overcome the limited data availability on intermittency and the difficulty of hydrological models in identifying the absence of streamflow, integrated approaches have been proposed, coupling hydrological modeling with other information such as interviews (Gallart et al., 2012), photos (Mimeau et al., 2024), citizen science apps (Truchy et al., 2023), or satellite images (Cavallo et al., 2022, 2025; De Girolamo et al., 2022; Gao et al., 2021). In this context, De Girolamo et al. (2022) utilized the SWAT model, combined with 24 high-resolution Google Earth satellite images (spatial resolution < 1 m), to determine the threshold flow rate corresponding to zero-flow event conditions (i.e., ponding or dry conditions). Although these images offer great spatial detail, their availability is limited in time, as they are occasional acquisitions. In contrast, the Sentinel-2 (S2) satellite mission provided by the European Space Agency (ESA) offers much more frequent time coverage (every 5 days). Still, it presents drawbacks for application in small headwater streams due to the sensor spatial resolution (10 m). Nevertheless, S2 imagery has shown an increasing use in monitoring aquatic resources (Cavallo et al., 2021a, 2021b; Kantharajan et al., 2022; Seaton et al., 2020). Recently, Cavallo et al. (2022) showed that using a specific combination of bands (SWIR-NIR-RED), S2 data can be effectively used to detect the presence of water along NPRs with an active channel width of 30 m or more and without vegetation cover (Costigan et al., 2017; Jiang et al., 2014). In this way, they obtained an evaluation of the frequency and duration of the FCs in NPRs.

This work seeks to integrate a Karst-SWAT hydrological model with S2 imagery to predict zero-flow events and estimate the hydrotype of the Keritis River (Greece). Hydrological modeling was used to predict daily streamflow, whereas S2 imagery provided river FCs with a revisit time of about 5 days. Using S2 data, two threshold streamflow rates were established to distinguish between the three different FCs (F, P, and D). The resulting FCs' frequencies allowed us to retrieve daily information on F, P, and D days, and thus to identify the relevant hydrotypes.

2. Study area

The study was conducted on two different river reaches of the Keritis River situated in the Chania Regional Unit of Crete, Greece (Fig. 1a). The Keritis River originates in the southern highlands of the White Mountains, near Mount Lefka Ori, and extends northward, discharging into the Cretan Sea. The Keritis Basin covers an area of approximately 278 km^2, with a river network extending for about 77.1 km. The watershed has a hot-summer Mediterranean climate, characterized by a dry season from May to October (Beck et al., 2018; Peel et al., 2007), with an average annual temperature of 19.96°C (Papafilippaki et al., 2008). The mean annual rainfall at the basin scale in the period 1974–2021 is 1098 mm (data extracted from rainfall stations), and it is usually concentrated in the mountainous areas, where it can reach up to 2000 mm instead of 665 mm in the coastal and low area of Chania (Chartzoulakis et al., 2001). Despite the relatively high annual precipitation, concentrated mainly during the winter season, the island experiences substantial evapotranspiration losses, accounting for approximately 65% of the annual rainfall. Only about 21% of precipitation contributes to

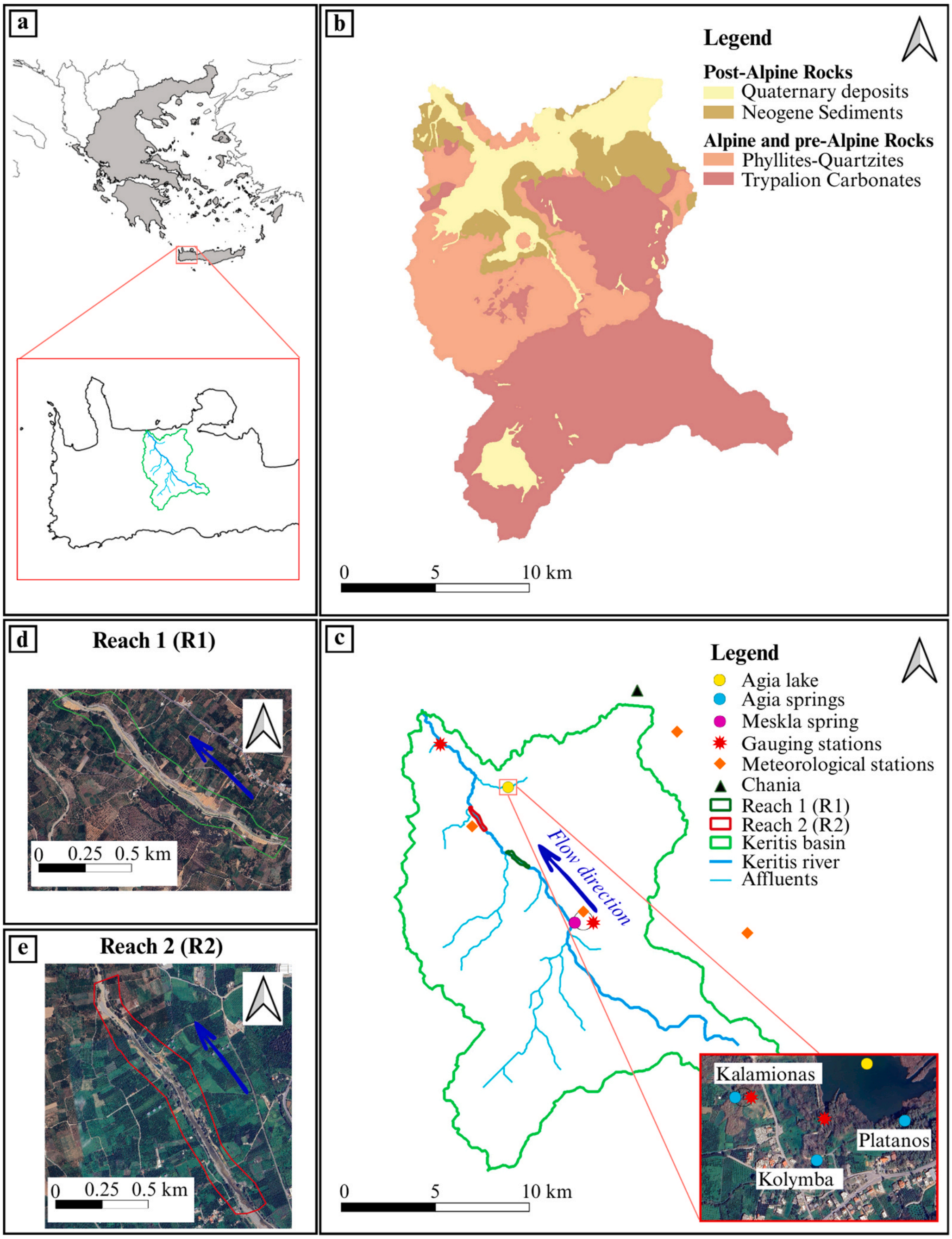

Fig. 1. (a) Location of the study area on Crete Island (Greece). (b) Lithological map of the Keritis Basin. (c) Hydrological network of the Keritis Basin, with a zoom-in of the Agia Lake karst system (connected symbols remain in the same position). (d) Detailed view of the reach R1. (e) Detailed view of the reach R2. Blue arrows indicate flow direction in panels (c–e). Map data: Google, ©2024–2025 Google, Airbus. Basemap created with QGIS 3.32.0.

surface runoff reaching the sea, while the remaining 14% recharges the groundwater system (Chartzoulakis et al., 2001; Chartzoulakis and Psarras, 2005). The investigated river reaches, defined as reach 1 (R1, upstream; Fig. 1d) and reach 2 (R2, downstream; Fig. 1e), exhibit partial artificial confined banks with a straight morphology (Rinaldi et al., 2016) and were selected as representative of the intermittent network of the Keritis River, with sufficient channel width and good satellite visibility (Table 1).

The geological framework of the Keritis Basin comprises two main lithological groups (Fig. 1b): Alpine-pre-Alpine and post-Alpine rocks. The Alpine and pre-Alpine rocks include Trypolis Carbonates, Trypalion Carbonates, Phyllites-Quartzites, and Plattenkalk Limestones. The post-Alpine rocks encompass Quaternary deposits and Neogene sediments. Distinct hydrogeological and hydraulic behaviors characterize the geological formations within the Keritis Basin. There are two main deeper hydrogeological systems and a secondary surface system (Nikolaidis and Karatzas, 2010; Perleros and Vozinakis, 2002). The deeper system, located predominantly in the southeast part of the basin, features impermeable carbonate formations. The second significant hydrogeological system is characterized by an impermeable formation of phyllites and schists, extending over the central part of the basin. The secondary hydrogeological system, consisting of Quaternary deposits north of the phyllites in the central part of the basin, is sustained by surface runoff from the phyllites and underground lateral flows east of the basin (Kourgialas et al., 2010; Nikolaidis et al., 2013; Steiakakis et al., 2023). The karstic formations in the area add complexity to the hydrogeological behavior of the watershed, giving rise to two deep hydrogeological systems that contribute to the Keritis River: the Meskla Spring in the central part of the basin and the karst system around the artificial Lake of Agia in the upper part that includes the karstic springs of Kalamionas, Platanos and Kolymba (Fig. 1c). The karst springs are crucial water supplies for drinking and irrigation purposes in the prefecture and contribute significantly to the Keritis River discharge (Nerantzaki et al., 2020). The area has four weather stations located in Alikianos, Meskla, inside the basin, and Agrokipio and Psychro Pigadi, outside it (Fig. 1c). A temporary gauging section for measuring the river flow rate was installed downstream, where all the karst contributions come together on the river channel (Fig. 1c). Flow measurements from the karstic springs were taken at different times at three locations: one at the Meskla spring and two within the Agia karst system – one specifically at the Kalamionas spring and another encompassing the total discharge from all Agia springs (Fig. 1c).

3. Material and methods

3.1. Methodological steps

To summarize the methodology applied in this study, a flowchart is provided in Fig. 2. Steps 1a and 1b describe the data collection process, where Sentinel-2 (S2) imagery between 2019 and 2023 was gathered for classification, while hydro-meteorological, geological, digital elevation model (DEM), land use, and soil type data are collected as input for hydrological modeling. In Step 2a, a supervised visual classification of the satellite images is performed to determine the Flow Conditions (FCs) of the river reaches as flowing (F), ponding (P), or dry (D). In Step 2b, the collected datasets were used to calibrate and validate the hydrological model, which is then applied to simulate a daily streamflow time series for the investigated reaches from 1971 to 2023. Step 3 couples the classified satellite data with the simulated flow rates for corresponding dates to identify the flow rate thresholds for distinguishing between F and P, and between P and D conditions. These thresholds serve as references in Step 4 to predict the FC for days without satellite observations. Finally, in Step 5, the permanence of the daily FCs - permanence of flowing (Mf), ponding (Mp), and dry (Md) - is used to determine the hydrotypes of the investigated reaches Non-Perennial Rivers (NPRs, Munné et al., 2021).

3.2. Data analysis

3.2.1. Satellite data

Selecting an appropriate procedure for monitoring hydrological processes in NPRs requires careful consideration of multiple factors, including spatial and temporal resolution as well as data availability (Gilvear and Bryant, 2016). Spatial resolution is particularly critical, as it determines the ability to detect and analyze specific hydrological features. Temporal resolution is equally important, as it aligns with the rate of change of the observed process (Boothroyd et al., 2021). In NPRs, transitions between FCs can exhibit highly complex spatial patterns and occur over short timescales; thus, the revisit time should be proportionally short. Among the freely available multispectral satellite missions that provide systematic global coverage, S2 stands out due to its good trade-off between spatial, spectral resolution, and revisit frequency. For this reason, this satellite dataset was selected for this work. The S2 mission, part of the Copernicus Earth Observation program managed by the ESA, comprises two twin satellites, Sentinel-2A (S2A) and Sentinel-2B (S2B), which share the same orbit and provide multispectral coverage of the Earth's surface. S2A was launched on June 23, 2015, followed by S2B on March 7, 2017. Before the launch of S2B, the revisit interval was ten days; since March 2017, with both satellites operational, this interval has been reduced to a maximum of five days, significantly enhancing the data acquisition frequency. Satellites 2 C, already in orbit, and 2D will replace S2A and S2B to ensure mission continuity. Each satellite carries a Multispectral Instrument (MSI) that captures images across 13 spectral bands. Among these bands, B2, B3, and B4 in the visible spectrum (VIS), and

Table 1
Length, average width, slope, and morphological type of the investigated reaches, R1 and R2, of the Keritis River.

Reach	Length (m)	Average width (m)	Slope	Morphology
R1	1480	30	0.01	Partially artificial, confined, straight
R2	1530	40	0.01	Partially artificial confined, straight

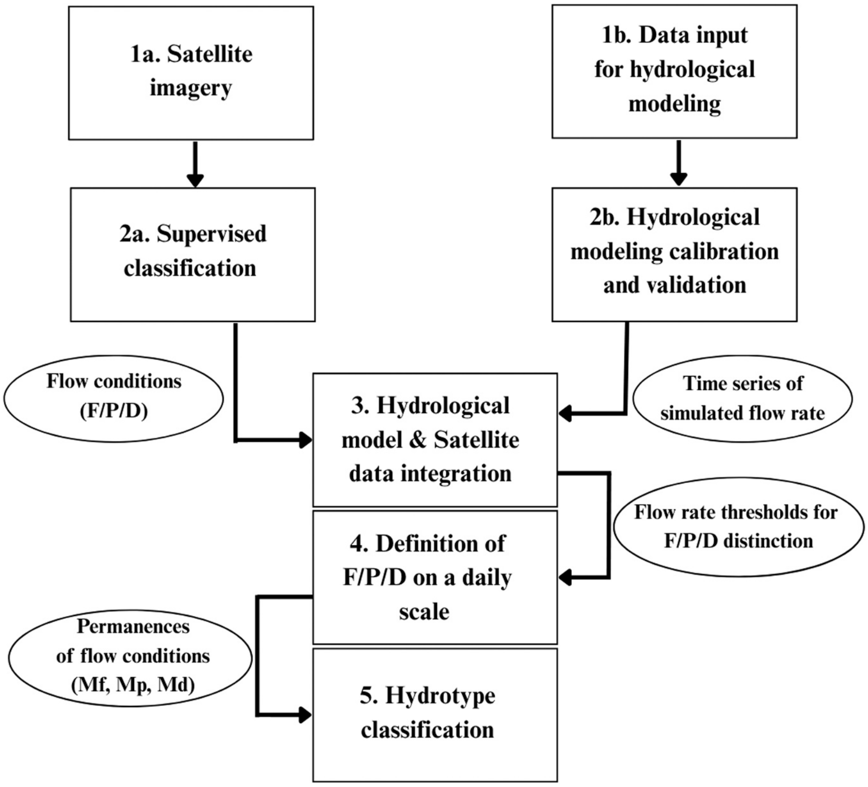

Fig. 2. Flowchart of the methodological steps. Steps 1a and 1b represent data collection of satellite imagery (Section 3.2.1) and hydrological model inputs (Section 3.2.2), respectively. Steps 2a and 2b correspond to the supervised classification of satellite imagery (Section 3.2.1) and the calibration and validation of the hydrological model (Section 3.2.2). Step 3 involves estimating the threshold values (Section 3.3). Step 4 refers to the determination of daily flow conditions (FCs), and Step 5 presents the identification of hydrotypes based on the three metrics (Mf, Mp, Md) (Section 3.4).

band B8 in the near-infrared (NIR), have a spatial resolution of 10 m. Additional bands with 20-meter resolution include bands B5, B6, and B7 in the Red-Edge spectrum, B8a in the narrow NIR, and B11 and B12 in the short-wave infrared (SWIR). For this study, S2 imagery was analyzed between March 2019 and December 2023. Earlier years and the first months of 2019 were excluded because vegetation cover hindered the ability to observe the active channel. S2 imagery, pre-processed to the bottom-of-atmosphere (i.e., Level-2A), was retrieved from the Copernicus Open Access Hub. Following the methodology outlined by Cavallo et al. (2022), False-Color Images (FCIs) were classified using Band 11, Band 8, and Band 4 (SWIR-NIR-RED), a combination that enhances the distinction between water and other characteristic features of a river channel, such as vegetation and sediments. To ensure consistency, the supervised classification was conducted through the Google Earth Engine algorithm (Cavallo et al., 2022) at a uniform scale of 1:10000. The classification process assigns each image into one of the three FCs: flowing (F), where a continuous water surface is visible along the channel; ponding (P), where water is present but discontinuous, forming isolated ponds or pools or submerged portions of the low-flow channel; and dry (D), where no visible surface water is detected and the riverbed is completely dry. Cloudy images were identified and excluded from the analysis. The classified dataset was subsequently analyzed by calculating the percentage of images classified for each FC relative to the total number of valid images, excluding those affected by cloud cover. In addition, the Effective Revisit Time (ERT) was computed as the ratio of valid images to the total number of days. This metric was then compared to the nominal revisit time of the S2 mission.

Four high-resolution images, provided by Google Earth Pro, acquired on 3rd March 2019, 5th May 2021, 3rd June 2022, and 17th April 2023, were used to identify shadows of vegetation and shadows of the banks that could be mistaken for water surfaces. In these cases, the FC classifications were corrected accordingly.

3.2.2. Hydrological modeling

To set up the SWAT model, a DEM with a spatial resolution of 0.025 km, a CORINE land use map, and a digital soil map with a 1 km resolution from the Harmonized World Soil Database (HWSD) (Nachtergaele et al., 2008) were used. The Keritis Basin is predominantly rural, with no point pollution sources, while land management practices are implicitly represented through the Curve Number values assigned to each land use class at the HRU level. Moreover, long-term climatic statistics for solar radiation, relative humidity, and wind velocity were implemented in the SWAT Weather Generator (WGN) database to characterize long-term climatic conditions, generate the corresponding meteorological variables, and fill gaps in incomplete records when required. Temperature and rainfall data were retrieved from four meteorological stations between 1961 and 2023 (see Fig. 1).

Streamflow data were used for calibrating and validating the model. These data are available at four points: one located along the downstream section of the Keritis River, one at the Meskla spring, two within the second karst system: in the Kalamionas spring and the overall discharge of the Agia springs (see Fig. 1). The temporary gauging station, which measured river stage, operated in the Keritis River over two distinct periods: from December 2012 to June 2013 and from December 2014 to June 2015. Flow measurements were conducted to establish a rating curve. The location of the gauging station is particularly significant because it is positioned in a downstream river section where all the contributions from karstic springs are integrated into the discharge. At that point, the Keritis River is perennial. For the Meskla springs, flow data are available from 9 January 1978–8 January 2005, whereas for the total Agia springs, the records cover 9 January 1978–8 January 1985. The Agia springs dataset refers to the collective flow of Kolymba, Platanos, and Kalamionas. Additionally, specific data for the Kalamionas spring span from 9 January 1971–8 January 1979.

Hydrological modelling of NPRs is particularly challenging due to the limited availability of hydrological monitoring data associated with their ephemeral nature. These challenges are further intensified in complex hydromorphological settings, such as Mediterranean karstic environments, where surface and subsurface flow pathways are highly interconnected and difficult to characterize. Under such conditions, reliable hydrological simulations require the integration of all available data sources together with local knowledge of existing hydrological pathways. The characteristics of the case study necessitated the application of a combined approach involving both the karst model and the SWAT model. The karst model specifically targeted the simulation of karstic formations. The SWAT model represents a hydrological model designed with precision to assess the impact of land management techniques on water resources. Developed under the guidance of the United States Department of Agriculture (USDA, Neitsch et al., 2011), SWAT distinguishes itself as a process-oriented, spatially distributed model adept at simulating various facets of the hydrological cycle (Arnold et al., 1998). These facets include precipitation, runoff, evapotranspiration, soil moisture, and nutrient transport. Operating at the watershed scale, the model enables a detailed assessment of the impacts of land use changes, climate variability, and management practices on both the quantity and quality of water resources. First, the watershed is divided into sub-catchments, and then each sub-catchment is split into hydrologic response units (HRUs) that are a function of soil type, land use, and land slope. The SWAT model operates continuously in time and does not simulate detailed flood routing for individual events. It is imperative to highlight that the SWAT model fails in simulating karst formation. This constraint is based on the underlying assumption of the SWAT model, where water exceeding the deep aquifer is considered lost from the system. However, in a karstic formation, water from the deep aquifer plays a crucial role as it contributes to the main river flowing through a pothole (Nikolaidis et al., 2013; Tzoraki and Nikolaidis, 2007). To address this limitation, the karstic model is introduced to retrieve the water from the deep aquifer and to direct it into two reservoirs. In addition, the Meskla karst springs contribute to the primary flow of the Keritis River but also supply water to the Agia karst formation. Consequently, there is a dual application of the karstic model. The Karst-SWAT modelling approach has been extensively applied in Mediterranean karstic watersheds (Nikolaidis et al., 2013) and successfully extended to regional-scale applications (Malagò et al., 2016), demonstrating its ability to represent the dominant hydrological pathways of such complex systems.

The first step in the modeling procedure was the collection of the necessary data, followed by the setup of the SWAT model and the calibration of the four springs. Finally, the total flow rate of the Keritis River was estimated. In all karstic sub-basins, the parameter representing the percentage of water reaching the deep aquifer was set to 1, meaning that 100% of the water discharge recharges the deep aquifer. The calibration methodology followed a five-step approach.

Step 1: The SWAT model was set up by importing the datasets collected for hydrological modeling.

Step 2: The sub-basins supplying the karstic formation feeding the Meskla spring were identified. The karst model was applied, and the amount of water flowing to the Agia karst reservoir was defined. Calibration and validation were performed using discharge data from the Meskla spring.

Step 3: The sub-basins supplying the karstic formation of Agia springs were identified, and the karst model was applied, followed by calibration and validation using discharge data from 1978 to 1985.

Step 4: The sub-basins supplying the karstic formation of Kalamionas spring were identified, and the karst model was applied, followed by calibration and validation using discharge data from 1971 to 1979.

Step 5: The total river discharge resulted from the sum of the surface flow of the river obtained from the SWAT model, the karstic discharge from the Meskla spring and the Agia system obtained from the karst model. Finally, the discharge data between 2012 and 2015 at the downstream section of the Keritis River were used for validation. It is important to note that withdrawals from the springs were excluded before the final comparison.

The five-step calibration procedure described above reflects a sequential modeling strategy dictated by the availability of streamflow observations for each karst spring and for the main river channel. Each calibration and validation step was performed independently within the corresponding observation period, and the model was not run as a single continuous simulation from 1971 to 2023. The objective of this approach was not the detailed reproduction of individual hydrological events, but the generation of physically consistent daily streamflow estimates suitable for coupling with satellite-derived flow condition classifications. A detailed description of the calibration strategy and validation procedure is provided in Sections S1 and S2 of the Supplementary Materials. Additional methodological details and calibration parameters are also reported in the Supplementary Materials (Table S1).

Validation at each step was assessed using statistical indicators such as the Nash-Sutcliffe efficiency (NSE, Nash and Sutcliffe, 1970) and the root mean square error observations standard deviation ratio (RSR, Moriasi et al., 2007). To evaluate the tendency of overestimation or underestimation of simulated data, the percent bias (PBIAS, Gupta et al., 1999) was used. Moreover, the NSE estimator is applied to a logarithmic transformation of the observed and simulated flow rates (LNSE) that increases the relative weight assigned to low-flows (Pushpalatha et al., 2012). Ultimately, the calibrated and validated model was employed to simulate the total discharge in the study reaches R1 and R2.

3.3. Integration between satellite data and hydrological modelling

Hydrological models tend to overestimate the discharge during extremely low FCs and fail to represent the absence of surface runoff correctly. Therefore, in the present work, simulated discharge data for the period between 2019 and 2023 were systematically compared with the corresponding FCs (F, P, and D) derived from the supervised classification of satellite imagery for each available date. To determine the discharge threshold value at which a river shifts from F to zero-flow (Threshold 1, T1), as well as the threshold at which a transition between P and D occurs (Threshold 2, T2), a Classification and Regression Tree (CART, Breiman et al., 1984; Kotsiantis, 2013) was employed. Specifically, using DecisionTreeClassifier from the scikit-learn Python library (Garreta and Moncecchi, 2013; Lamrini, 2020), we determined the most suitable threshold values (T1 and T2). This algorithm is widely used in water sciences (Dehghani et al., 2023) for water quality analysis (Gakii and Jepkoech, 2019; Jaloree et al., 2014) or for improving variable selection for hydrological models (Galelli and Castelletti, 2013). In particular, a Decision Stump (DS, a decision tree with a depth of 1 internal node) was used, which represents a very simple form of the CART. The DS was employed to determine, for each year, the optimal threshold values (T1 and T2) by analyzing the distribution of discharge values and identifying the optimal split point between F and zero-flow events (T1) and between P and D (T2). Before classification, an oversampling step using the Synthetic Minority Over-sampling Technique (SMOTE, Chawla et al., 2002) was employed, limiting common issues with unbalanced datasets (Mohammed et al., 2020).

Due to the significant temporal variability that affects flow intermittency (Magand et al., 2020), for each year and for each threshold (T1 and T2), a separate DS was trained. Accuracy and True Skill Statistic (TSS, Allouche et al., 2006) were used to assess the reliability of the identified thresholds in defining hydrological transitions across different years.

3.4. Hydrotype identification

The classification of river hydrotypes serves as a crucial preliminary step in ecological status assessment and the subsequent application of appropriate management actions. The simulated flow rate time series between 2019 and 2023 were used to classify FCs for days with no corresponding classified S2 imagery. Once the threshold values T1 and T2 were defined, the method employed a two-step binary algorithm (schematized in Fig. 3). In the first step, days with flow rates exceeding T1 are identified as F, while all others are classified as zero-flow events. In the second step, zero-flow events are further distinguished: flow rates above T2 are classified as P, whereas those below T2 are considered D.

The permanence of daily FC is, then, measured by Mf (permanence of flowing), Mp (permanence of ponding), and Md (permanence of dry).

According to Munné et al. (2021), a ternary plot, with Mf on the left axis, Mp on the right axis, and Md on the bottom axis, was used to determine the hydrotype of each NPR reach. The four categories are: (1) Perennial or Quasi-Perennial (Qp) river, where the F condition is predominant; (2) Intermittent-fluent (If), characterized by a more balanced permanence of F and zero-flow events; (3) Intermittent-stagnant (Is) identifies rivers where P is the most common condition and (4) Ephemeral (Ep) occurs when the D condition is prevalent. The intervals of Mf, Mp, and Md that characterize each hydrotype are reported in Table 2.

Finally, a comparison is performed between the permanence metrics (Mf, Mp, and Md) derived exclusively from the classified S2 imagery and those obtained by simulated flow rates at a daily scale. This assessment evaluates the consistency between the two

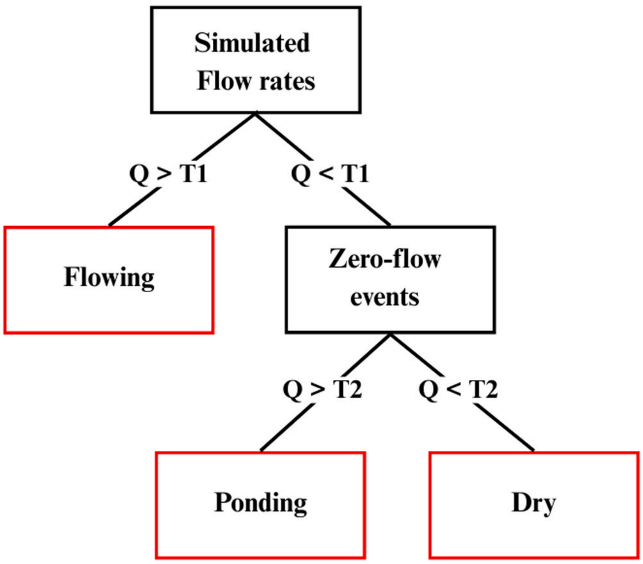

Fig. 3. Schematic representation of the two-step binary algorithm used for assigning the corresponding flowing condition to each simulated daily flow rate.

datasets.

3.5. Error assessment

A classification error analysis was adopted to evaluate how hydrotype identification is affected by the definition of zero-flow thresholds and by the supervised classification of the S2 imagery, when only a limited number of high-resolution images and no ground-truth data are available. Specifically, the analysis was designed to assess both the consistency of the supervised classification of the S2 dataset and the error of the integrated approach in estimating Mf, Mp, Md metrics, and the relative hydrotype.

The analysis was based on the use of parallel remote sensing data acquired from the PlanetScope (PS) constellation. PS is a commercial constellation operated by Planet Labs (San Francisco, California, USA), consisting of approximately 150 CubeSat satellites in sun-synchronous orbit launched in 2013. The satellites are equipped with optical sensors acquiring imagery in the visible and NIR spectral ranges. Owing to the large number of satellites, the constellation provides a very high temporal resolution (approximately daily revisit time) and a spatial resolution of about 3 m (Frazier and Hemingway, 2021; Roy et al., 2021).

Although PS imagery cannot be considered ground-truth data, its substantially higher spatial resolution and daily revisit frequency provide an independent high-resolution reference dataset suitable for assessing classification uncertainty.

Therefore, a two-year classification was performed using all the cloud-free images available through the Planet Explorer platform (https://www.planet.com/explorer/). It is important to note that, compared to S2, PS data are not freely available and are subject to limitations on the number of images that can be downloaded per month for educational or research purposes. These constraints limit the possibility of an extensive and generalized use of PS imagery for estimating zero-flow events in NPRs, but can be used to assess the classification error derived from S2 data.

The error analysis had two main objectives: (i) to compare PS and S2 classifications on days when cloud-free images were available for both datasets, to have an evaluation of the uncertainty associated with supervised S2 classification; and (ii) to assess the error of the integrated approach in predicting F, P, and D conditions on days without valid S2 imagery.

To classify the PS dataset, all clipped images were downloaded and processed using GIS tools and a Google Colab environment by performing an image-by-image supervised classification at a uniform scale of 1:10000, following the approach adopted for S2 data. Due to the absence of the SWIR band in PS imagery, the Blue band was used. Although it does not provide the strong water absorption properties of SWIR, the Blue band exhibits relatively reduced reflectance over water compared to surrounding dry substrates, supporting visual discrimination of FCs.

Confusion matrices were computed for reaches R1 and R2 by comparing the F, P, and D classes derived from PS with those obtained from S2 and from the integrated approach. Overall Accuracy (OA) and TSS were then calculated to quantify classification performances in both cases.

The misclassification rate ($1 - \mathrm{OA}$) was used as a conservative estimate of classification error and represented as a circular buffer around the points in the ternary plot. The radius (r) is calculated as:

$$\mathrm{r} = (1 - \mathrm{OA}) \bullet 100 \tag{1}$$

4. Results

4.1. Sentinel-2 data analysis

The study analyzed two distinct reaches, R1 and R2, over a period extending from March 2019 to December 2023. Fig. 4 shows the False-Color Images (FCIs) of the Reach 1. In this combination, water appears in black or dark-blue color, vegetation in green, and bare soil or sediments in light pink or white. The Figure illustrates how different flow conditions (FCs) can be clearly distinguishable in the FCIs.

A total of 349 and 350 images for R1 and R2 were examined to assess different FCs within the study area. Additionally, Table 3 displays the number of S2 acquisitions available for each year in the two study reaches. The same table also shows the number of images that were discarded due to cloud cover. This allows the effective revisit time (ERT) to be calculated, which results in an average of 8.66 and 8.30 days for R1 and R2, respectively.

An analysis of the classification results (Fig. 5) reveals that the two river reaches have similar trends, but with longer dry and zero-flow periods in R1. The F condition occurs on average for half of the observations, but with significant fluctuations from one year to the next, with a minimum in 2023 (10.53% of observations in R1 and 40.00% in R2) and a maximum in 2020 (68.75% in R1 and 75.00% in

Table 2
Criteria for distinguishing between non-perennial river hydrotype using the three permanence values (Mf, Mp, and Md, details in Munné et al., 2021). Mf, Mp, and Md represent the percentages of permanence for flowing, ponding, and dry conditions.

Hydrotype	Mf (%)	Mp (%)	Md (%)
Perennial or	$99 < \mathrm{Mf} \leq 100$	$0 \leq \mathrm{Mp} < 1$	$0 \leq \mathrm{Md} < 1$
Quasi-perennial	$82 < \mathrm{Mf} \leq 100$	$0 \leq \mathrm{Mp} \leq 18$	$0 \leq \mathrm{Md} \leq 18$
Intermittent-fluent	$27 < \mathrm{Mf} \leq 82$	$0 \leq \mathrm{Mp} \leq 73$	$0 \leq \mathrm{Md} \leq 73$
Intermittent-stagnant	$0 < \mathrm{Mf} \leq 27$	$40 \leq \mathrm{Mp} \leq 100$	$0 \leq \mathrm{Md} \leq 60$
Ephemeral	$0 < \mathrm{Mf} \leq 27$	$0 \leq \mathrm{Mp} \leq 40$	$33 \leq \mathrm{Md} \leq 100$

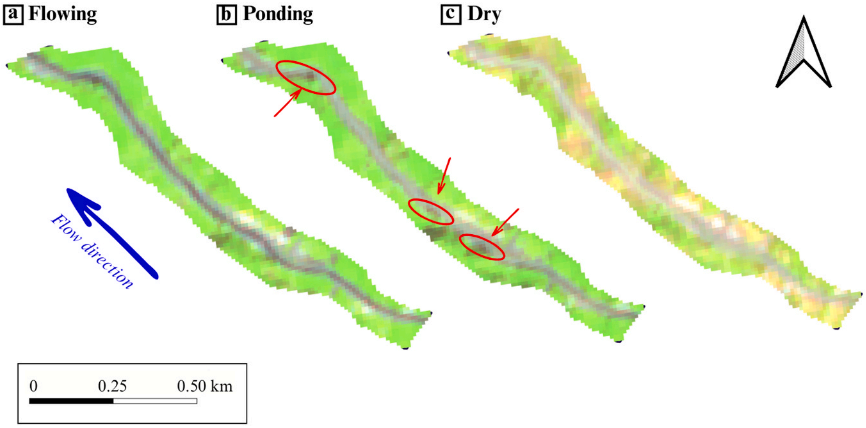

Fig. 4. Sentinel-2 False-color images (FCIs, B11-B8-B4) of the three different flow conditions (FCs) for Reach 1: a) Flowing condition on 26th March 2023, represented by a continuous dark line inside the riverbed. b) Ponding condition on 25th January 2023; red arrows and ovals highlight the isolated ponds, represented by dark areas inside the riverbed. c) Dry condition on 14th July 2023.

Table 3
Overall classified images, images classified as cloudy, and Effective Revisit times (ERTs) of Sentinel-2 images for reaches R1 and R2, between March 2019 and December 2023. ERT is the effective frequency in days of valuable images for detecting flow conditions.

		2019	2020	2021	2022	2023	Overall
	Classified images	57	73	73	73	73	349
R1	**Cloudy images**	20	25	32	33	35	145
	ERT [days]	8.27	7.63	8.90	9.13	9.61	8.66
	Classified images	58	73	73	73	73	350
R2	**Cloudy images**	17	25	30	32	33	137
	ERT [days]	7.46	7.63	8.49	8.90	9.13	8.30

R2). The transition from F to zero-flow conditions typically occurred between late June and early July, while rewetting generally took place during the first half of October. D state was not observed every year (3 years out of 5 in R1 and 2 out of 5 in R2). The driest year for both reaches is 2023, with D state from the end of May until the end of October in R1, reaching 57.89%, and from mid-August to late October in R2, which presents a lower percentage than R1, around 30.00%. In the other years, the D condition was observed in less than 5% of cases and was concentrated in September and October. Before 2023, there was no year in which both reaches underwent D condition. Conversely, P is the dominant non-flowing condition, occurring about three times more frequently than D in R1 and more than five times in R2 during 2019–2023. Furthermore, the P condition is more stable and homogenous within the period 2019–2023, ranging between 27.08% and 53.66% for R1 and 25.00% and 43.90% for R2.

4.2. Hydrological modeling results

The performance of the model, illustrated in Table 4, for the karst springs was evaluated using the NSE, LNSE, RSR, and PBIAS indices, following the criteria proposed by Moriasi et al. (2007), (2015) for monthly time steps. For the Meskla springs, the calibration period (Jan 1982–Dec 1992) showed good to satisfactory model performance (NSE = 0.69, LNSE= 0.60, RSR = 0.56), with a moderate overestimation of discharge (PBIAS = −16.26%). During the validation period (Jan 1993–Aug 2005), model performance decreased to satisfactory to marginally acceptable levels, except for LNSE, which remains good (NSE = 0.54, LNSE=0.61, RSR = 0.68), accompanied by a stronger overestimation of flows (PBIAS = −31.8%). For the Agia springs, the calibration period (Sep 1981–Aug 1985) yielded satisfactory performance (NSE = 0.5, LNSE=0.58, RSR = 0.71) with very low bias (PBIAS = −3.48%), indicating a good representation of mean discharge conditions. In contrast, the validation period (Sep 1978–Jun 1981) exhibited unsatisfactory performance (NSE = −0.52, LNSE= −0.2, RSR = 1.23), suggesting limited skill in reproducing the temporal variability of observed flows, despite the small overall bias (PBIAS = 2.59%). For the Kalamionas spring, calibration over the period Jan 1973–Dec 1976 resulted in satisfactory performance (NSE = 0.46, LNSE=0.44, RSR = 0.74) with a slight underestimation of discharge (PBIAS = 2.39%), whereas validation for Jan 1977–Dec 1978 was unsatisfactory (NSE = −1.18, LNSE= −1.62, RSR = 1.48), with a PBIAS of 11.07%, indicating a more pronounced underestimation of discharge during the validation phase. The reduced performance is primarily attributed to the short length of the validation period and the limited hydrological variability captured. Regarding the main Keritis channel, the validation results for the period Dec 2012–Jun 2013 (NSE = −1.01, LNSE=0.53, RSR = 1.42, PBIAS = −9.29%) indicate unsatisfactory model performance in terms of flow variability reproduction, as reflected by the negative NSE and high RSR values. However, the LNSE presents satisfactory performance and the PBIAS value (-9.29%) falls within the very good performance range, indicating an overall satisfactory representation of the overall discharge volume despite limitations in capturing the temporal dynamics, especially for high

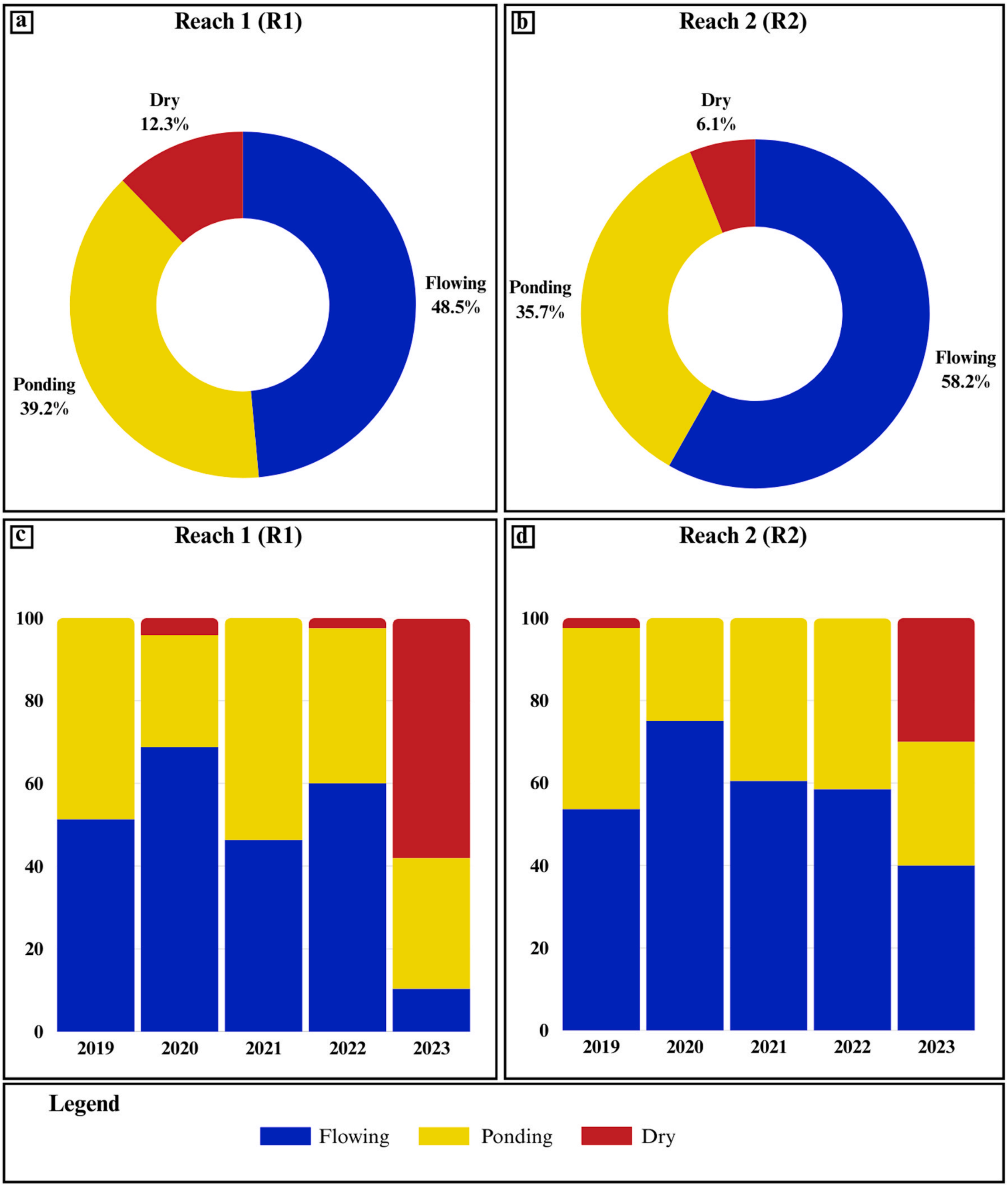

Fig. 5. Results of the supervised classification of the Sentinel-2 images. Results are reported for a) Reach R1 and b) Reach R2 in terms of the percentages of the total number of images classified as Flowing - F, Ponding – P, and Dry - D in the period March 2019 – December 2023; Percentage of each flowing condition for c) Reach R1 and d) Reach R2 for each considered year.

flows. Similarly, for the period Dec 2014–Mar 2015 (NSE = −0.55, LNSE=0.41, RSR = 1.25, PBIAS = −14.74%), the model performance remained unsatisfactory according to NSE and RSR and LNSE, even if the increase of values of LNSE compared to NSE highlight the better capacity in simulating low-flows. Nevertheless, the PBIAS value lies within the good range, suggesting acceptable agreement in terms of cumulative flow volume during this short validation interval.

Overall, the variability in model performance across calibration and validation periods reflects the inherent difficulty of simulating karst hydrological systems. Karst springs are characterized by highly heterogeneous subsurface structures, non-linear flow processes, and rapid responses to precipitation events, which are often not fully captured by conceptual or semi-distributed models. These

Table 4
Statistical indicators for the hydrological model validation step based on general performance ratings. The four indicators are: the Nash-Sutcliffe efficiency (NSE) and the logarithmic NSE (LNSE), root mean square error observations standard deviation ratio (RSR), and percent bias (PBIAS). The statistical indicators were evaluated on monthly-average discharge between 01/1993–08/2005 for Meskla spring, 01/1977–12/1978 for Kalamionas spring, 09/1978–06/1981 for Agia springs, 12/2012–06/2013 and 12/2014–03/2015 for Keritis main channel.

	NSE	LNSE	RSR	PBIAS [%]
Meskla spring	0.54	0.61	0.68	-31.8
Kalamionas spring	−1.18	-1.62	1.48	11.07
Agia springs	-0.52	-0.2	1.23	2.59
Keritis 2012-2013	-1.01	0.53	1.42	-9.29
Keritis 2014-2015	-0.55	0.41	1.25	-14.74

Very good	Good	Satisfactory	Unsatisfactory

complexities, combined with limited and discontinuous observational records, introduce additional uncertainty and partly explain the reduced performance during certain validation periods. Nevertheless, the results indicate that the adopted Karst-SWAT approach is able to reproduce the discharge volume and seasonal dynamics of spring discharge, providing a reasonable representation of karst groundwater contributions at the catchment scale. Fig. 6a-c presents the observed (red points) and simulated (blue line) monthly discharges for the Meskla, Agia, and Kalamionas karst springs during the respective validation periods, illustrating the model's ability to reproduce the seasonal variability and magnitude of spring flows, as well as the deviations observed during independent validation intervals. Fig. 6d-e presents the comparison between simulated and observed in the main channel of Keritis in the two different periods of measurements. Fig. 6f presents the final output, showing the time series of the total simulated Keritis daily flow rate at reach R1 and the corresponding rainfall over the period 2019–2023.

4.3. Integration between hydrological modeling and satellite data

The complete dataset, which includes the classified S2 images alongside the simulated flow rate, is provided in Table S2 of the Supplementary Materials for R1 and Table S3 for R2. Fig. 7a-b illustrates the time series of simulated flow rates for R1 and R2, represented on a log scale, alongside the corresponding FCs identified from S2 imagery.

The results demonstrate a clear transition from flowing conditions to zero-flow events and, in some cases, entirely dry conditions, as flow rates decrease. However, this relationship exhibits interannual variability.

Furthermore, the boxplots in Supplementary Figure S1a-b highlight the distinct distribution of flow rates associated with each FC for each year. These distinctions indicate a consistent pattern in the classification of FCs according to flow rate, both in years characterized by two conditions and in those that exhibit all three.

The Decision Stump (DS) was applied on a year-by-year basis to determine the thresholds reported in Table 5. The results highlight the interannual variability of the threshold values (T1 and T2) and the associated classification performance metrics for R1 and R2. The thresholds for distinguishing between F and zero-flow events (T1) exhibit fluctuations across different years. In R1, T1 values range from 0.59 m^3 /s in 2021–1.34 m^3 /s in 2022, while in R2, they vary from 0.55 m^3 /s in 2021–1.77 m^3 /s in 2022. These variations indicate that the transition between F and zero-flow events is not constant over time.

Despite this variability, the classification of F versus zero-flow events (T1) consistently achieves high accuracy, with values ranging from 0.90 to 1 across both reaches. Similarly, the True Skill Statistic (TSS) for T1 remains above 0.83 in most cases, confirming the robustness of the threshold-based classification.

T2, as well, shows interannual variability ranging from 0.27 m^3 /s in 2020–0.71 m^3 /s in 2023 for R1 and from 0.35 m^3 /s in 2019–0.46 m^3 /s in 2023 for R2. For those years in which no D condition was detected by satellite images, T2 was not defined.

The classification of P versus D conditions (T2) shows lower performance. Accuracy values for T2 range from 0.83 to 0.95, with lower TSS values compared to T1, particularly in R1.

Fig. 7c presents the number of zero-flow days (combining P and D days) obtained from the integrated approach for each year for both R1 and R2, compared to the annual water balance for the overall watershed obtained from the Karst-SWAT model. In 2019, despite more than 1800 mm of precipitation overall, a significant number of zero-flow days were observed: 153 days for R1 and 119 for R2. Two consecutive highly humid years, 2019–2020, led to lower values of zero-flow days in 2020, with 80 and 75, respectively. On the other hand, in the last three years, several droughts have occurred with zero-flow days between 160 and 289 days for R1 and 144

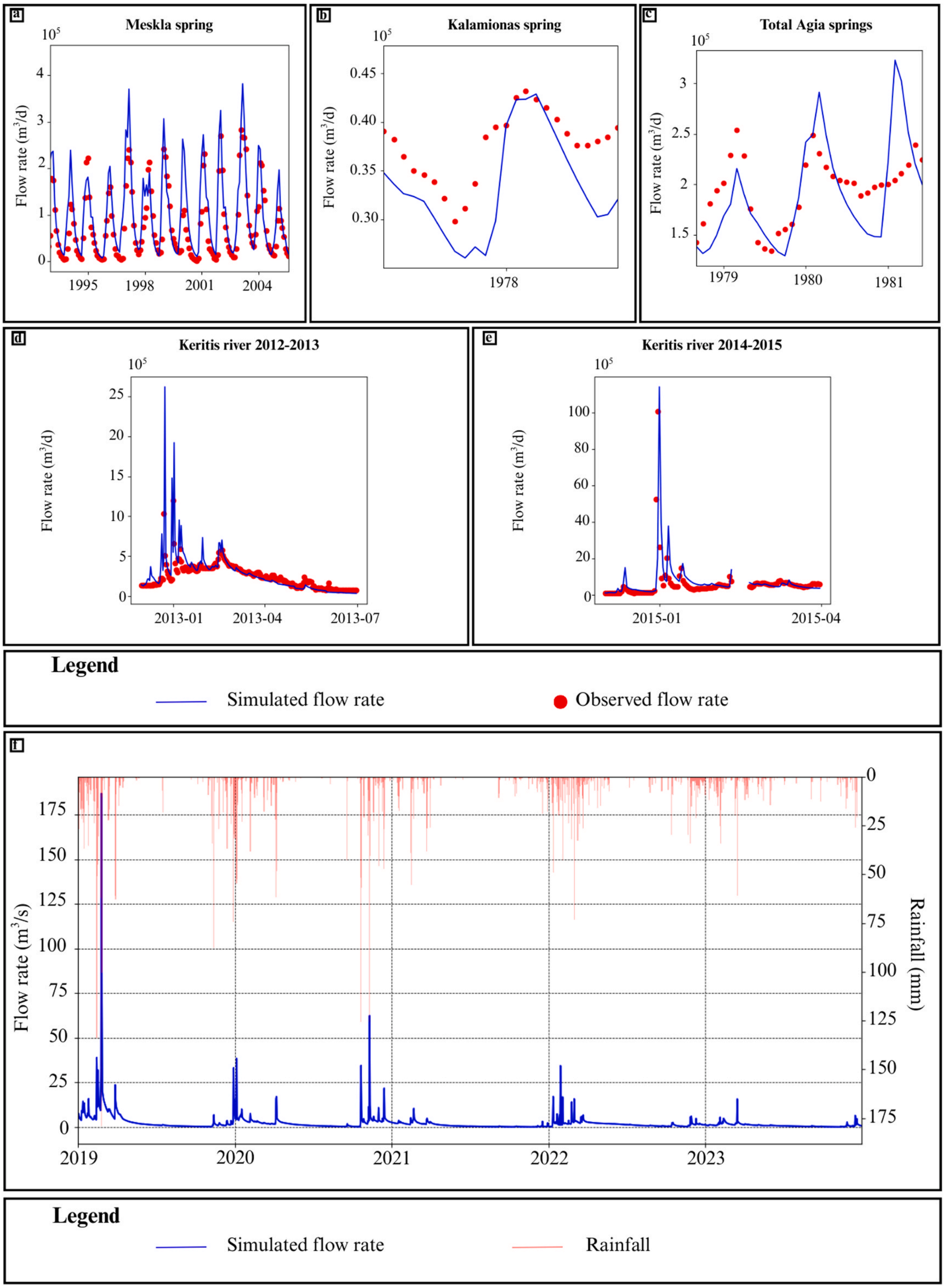

Fig. 6. Hydrological modeling validation steps. Comparison between observed (red points) and simulated monthly-average flow rates (blue line) from: a) Meskla spring (01/1993–08/2005), b) Kalamionas spring, part of the Agia system (01/1973–12/1976), c) total flow rate from Agia springs (09/1978–06/1981), d) total Keritis flow rate (12/2012–06/2013), e) total Keritis flow rate (12/2014–06/2015). In f), the subplot represents the timeseries of total flow rate in the Keritis River at reach R1 (in blue line, 2019–2023) and the rainfall (in red).

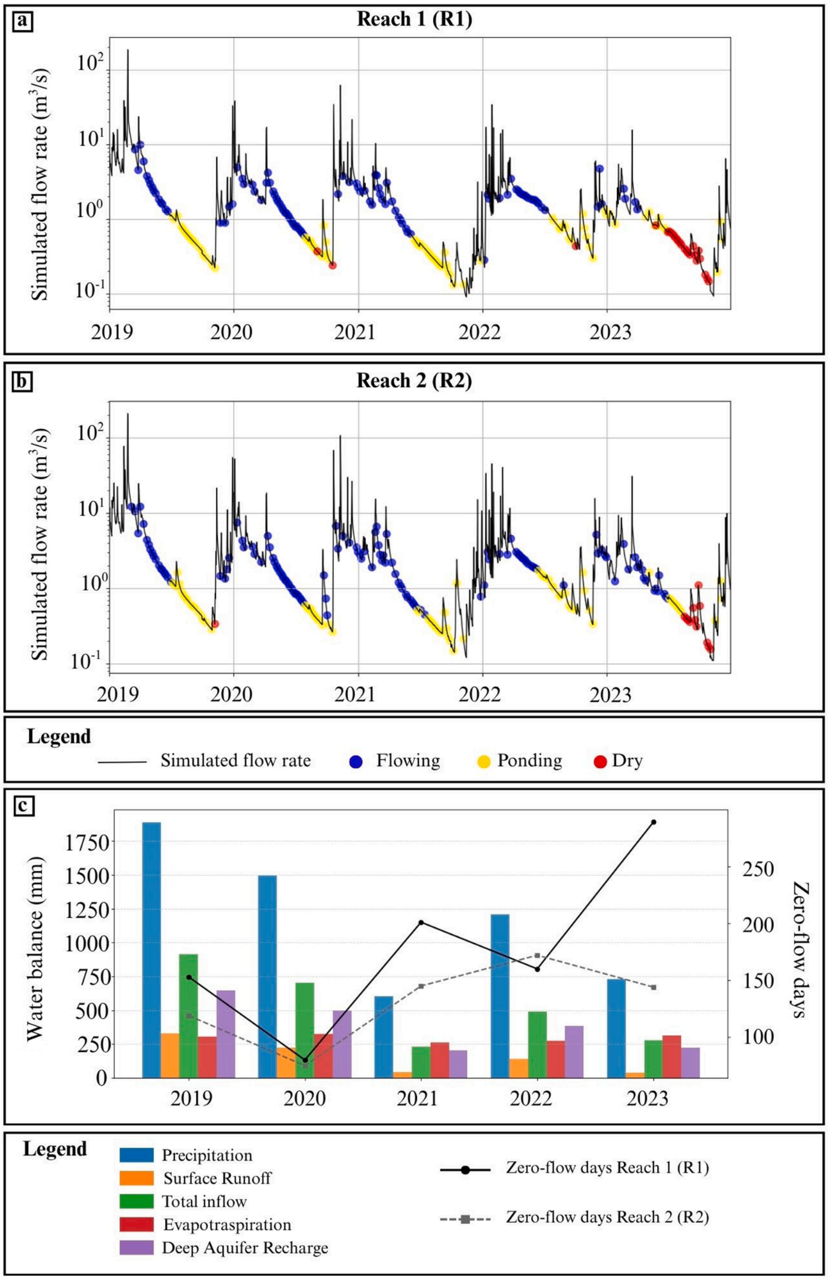

Fig. 7. Simulated flow rate (black line) time series in log scale with color-coded points representing satellite-detected Flow Conditions (FCs): blue for Flowing, yellow for Ponding, and red for Dry for both (a) reach R1 and (b) reach R2. (c) Water balance components at an annual scale for the overall watershed and corresponding zero-flow days obtained from the integrated approach for reach R1 and reach R2 for the period 2019–2023.

and 172 days for R2. While deep recharge provides a relatively stable but significant contribution, limiting the total inflow in Keritis River, representing between 34.30% and 30.66% of precipitation in 2019 and 2023, respectively, the Evapotranspiration (ET) contribution goes from 19.01% of precipitation on average between 2019 and 2020 to almost double of 36.41% on the last three years. In particular, in 2021 and 2023, ET exceeds 40% of annual precipitation and dominated the total inflow in absolute terms. These years show the highest annual combined number of zero-flow days across reaches R1 and R2.

4.4. Hydrotype identification and error estimation

The analysis of the PlanetScope (PS) dataset was exploited for the years 2020 and 2023, resulting in a total of 998 images, approximately 250 images per year per reach. Out of these, 552 were classified as cloudy, leading to an effective revisit time of less

Table 5
Identification of thresholds T1 and T2 for both river reaches R1 and R2 on a year-by-year basis and corresponding statistics of total accuracy and True Skill Statistics (TSS).

		T1 (m^3/s)	Accuracy	TSS	T2 (m^3/s)	Accuracy	TSS
	2019	1.19	0.95	0.89	-	-	-
	2020	0.60	0.98	0.93	0.27	0.88	0.87
R1	**2021**	0.59	1.00	1.00	-	-	-
	2022	1.34	0.98	0.96	0.48	0.93	0.50
	2023	1.32	1.00	1.00	0.71	0.91	0.79
	2019	1.22	0.98	0.95	0.35	0.95	0.94
	2020	0.63	0.98	0.97	-	-	-
R2	**2021**	0.55	0.93	0.83	-	-	-
	2022	1.77	0.95	0.92	-	-	-
	2023	0.74	0.90	0.83	0.46	0.83	0.67

than 3 days for both cases.

Fig. 8 shows the confusion matrices comparing S2 and the integrated approach with PS classifications for reaches R1 and R2. For the S2–PS comparison, very high agreement was observed. In R1 (Fig. 8a), the Overall Accuracy (OA) reached 0.96, with TSS values of 0.94 F, 0.90 P, and 0.97 D. In R2 (Fig. 8b), the OA was 0.95, with TSS values of 0.95 F, 0.85 P, and 0.92 D. Misclassifications were 2 out of 55 images and 3 out of 57, and mainly involved the P condition. The integrated approach also showed strong agreement with PS. In R1 (Fig. 8c), OA was 0.96, with TSS values of 0.92 F, 0.89 P, and 0.97 D. In R2 (Fig. 8d), OA slightly decreased to 0.92, while TSS values remained high for F (0.88) and D (0.92), and moderately high for P (0.76). The main discrepancies occurred between the F and P conditions.

The application of T1 and T2 on the daily time series of simulated flow rates for R1 and R2 allows for the shift from Mf, Mp, and Md (based on S2 imagery) to a permanence metric based on daily information. To distinguish the latter from those obtained exclusively from satellite imagery, we denote them with the subscript 'h'. For R1, the resulting permanence results in Mf_h= 51.64%, Mp_h= 37.13% and Md_h= 11.23%. On the other hand, for R2, the overall values are Mf_h= 63.96%, Mp_h= 30.67%, and Md_h= 5.37%. The comparison of daily simulated flow rates with T1 and T2 permits the identification of the FCs for every day within the period 2019–2023.

Figures S2a-b (see Supplementary Materials) highlight the temporal variability of the permanence indices (Mf_h, Mp_h, and Md_h) obtained from the integrated approach from year to year. This variability is particularly evident in R1, where the 2023 (in dark green) data point falls within a different region (Ephemeral) compared to the 2019–2022 points, which are in the Intermittent-Fluent region. In contrast, for R2, the variability does not lead to a shift from one hydrotype to another.

Fig. 9 illustrates the comparison between the permanence values obtained for the entire study period (2019–2023) through the supervised classification of S2 imagery (in yellow) and the results derived from the integrated approach using T1 and T2 (in red). Overall, for both R1 and R2, the hydrotype attribution derived from the supervised classification of S2 imagery and the integrated approach provides consistent results, both classifying R1 and R2 as Intermittent-Fluent and closely aligning. Moreover, for both river reaches, the Mf estimated solely from S2-classified images is lower than the Mf_h obtained from the flow rate simulations. However, in all panels (Figures 9a–b and S2a–b), the error-range remains entirely within the corresponding hydrotype region, indicating that classification errors do not alter the assigned hydrotype.

5. Discussion

This study presents a novel methodology that integrates Sentinel-2 (S2) imagery with a Karst-SWAT model to improve the identification of zero-flow conditions in Non-Perennial Rivers (NPRs) and the estimation of their hydrotype. A total of 699 False-Color Images (FCIs) from S2 imagery were analyzed between March 2019 and December 2023, of which 417 were cloud-free and usable for Flow Condition (FCs) classification. The average Effective Revisit Time (ERT) was therefore approximately 8.3–8.7 days. This is a crucial consideration given that the phenomenon under investigation undergoes rapid changes. Although cloud cover had a moderate impact, this temporal resolution remains insufficient to capture the rapid transitions between FC. These findings highlight the need for complementary data sources or techniques to determine the FC at a daily scale.

The hydrological modeling results highlight the limitations of the Karst-SWAT model in simulating daily streamflow in the Keritis Basin, where the dynamics are strongly influenced by karstic formations and constrained by limited data availability (Table 4). Looking at the results, the second karstic system, referring to Kalamionas plus Kolymba and Platanos springs, presents "Unsatisfactory" performances except for the PBIAS indicator. However, it is important to note that the studied reaches R1 and R2 are located upstream of this second karstic system, and are therefore mainly influenced by the first karst system (Meskla spring), for which "Satisfactory" performance was reached. The limitation in forecasting flow rate peaks, which strongly affects NSE, can be attributed to the complexity of simulating flow through Karst-SWAT conduits and the limited rainfall data in the upper part of the basin. Overall, the Karst-SWAT model reproduces the main hydrological patterns, including low-flow periods and peak events, but shows limitations in representing zero-flow conditions (Fig. 7a-b). This is consistent with existing literature indicating that conventional hydrological models, particularly when fed by limited data, tend to oversimplify or misrepresent the complex interplay of subsurface processes, especially in karst-influenced catchments, often overestimating flow rates during low-flows or zero-flow events (Kirkby et al., 2011).

Due to the moderate performance of the hydrological model, the integration with S2 imagery becomes essential. Traditional

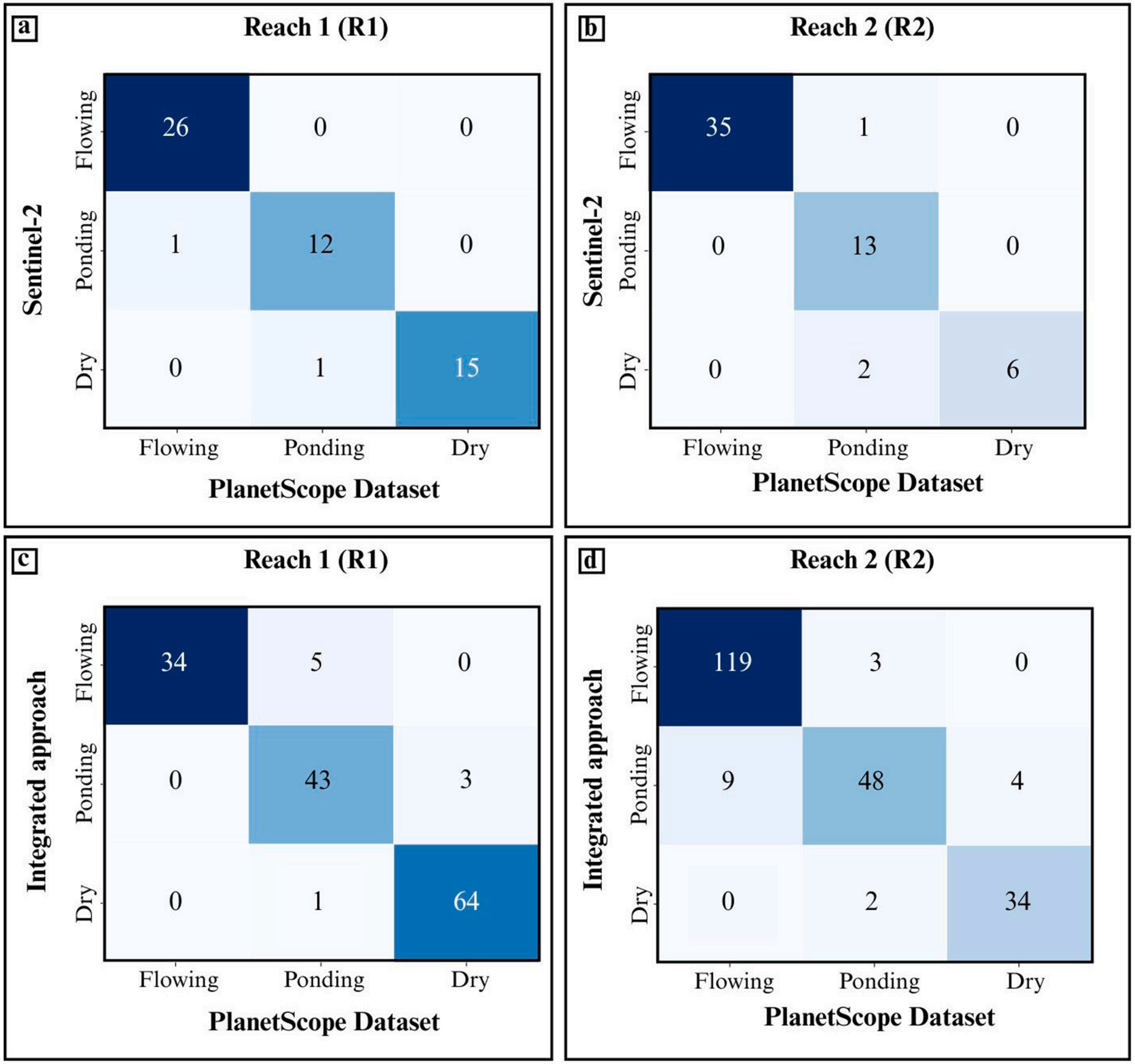

Fig. 8. Confusion matrices for reaches R1, comparing supervised classifications from Sentinel-2 and PlanetScope images acquired on the same day in 2020 and 2023 (a-b) and the resulting classification using the Integrated approach and PlanetScope (c-d).

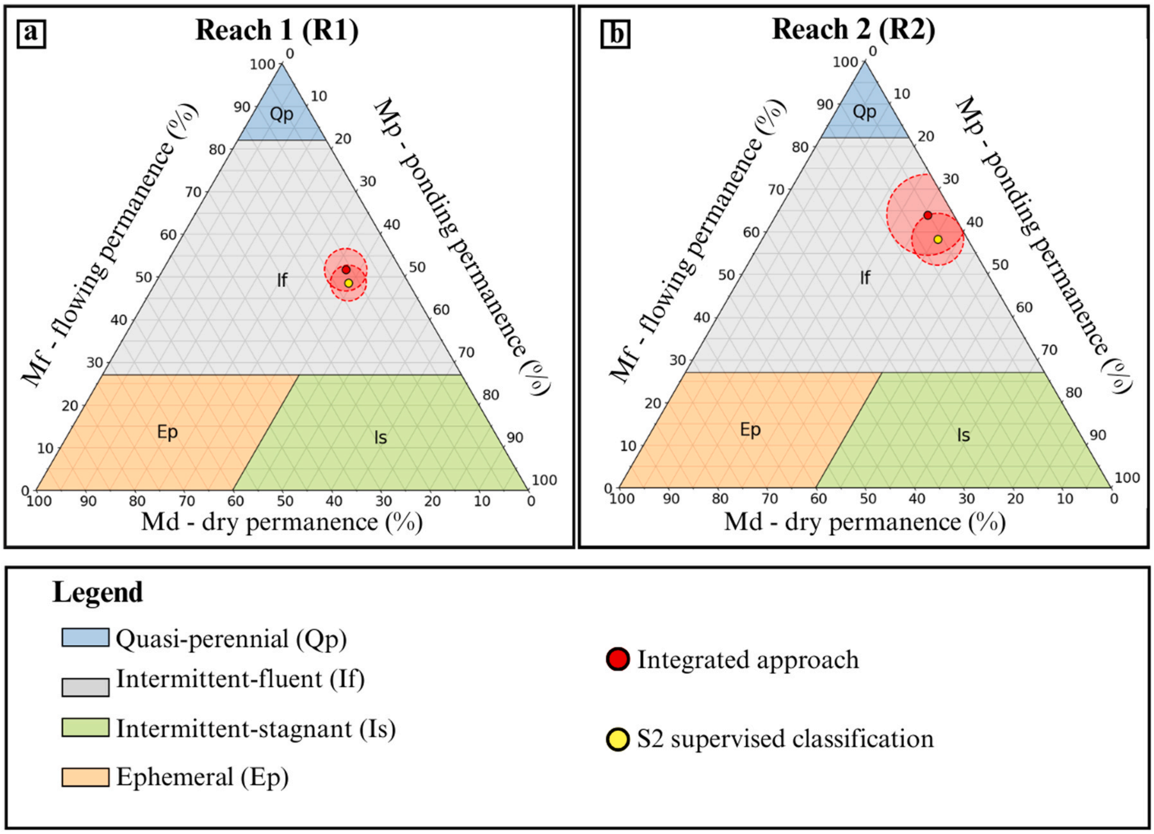

Fig. 9. Ternary plots for hydrotype identification in temporary rivers over the entire period (2019–2023) based on the supervised classification of Sentinel-2 (S2) imagery (in yellow) and the integrated approach (in red) with their associated error ranges.

gauging station data are often inadequate for describing drying phenomena, as stations are typically located in perennial reaches and poorly capture intermittency patterns (Zimmer et al., 2020; Krabbenhoft et al., 2022). Satellite observations, by contrast, provide spatially explicit information on the presence or absence of surface water, enabling the detection of intermittency patterns that cannot be fully represented by models or gauging data alone. This complementarity is particularly important in karst basins, where transitions between flowing and zero-flow events may be controlled by local variations in hydraulic conductivity, water table fluctuations, infiltration losses, or unrecorded water withdrawals. The results of this study demonstrate that hydrological modelling and remote sensing provide complementary information: the hydrological model ensures temporal continuity, while satellite imagery constrains the classification of surface water presence. The integrated approach enabled the estimation of zero-flow thresholds (T1 and T2), which were used to properly distinguish between the different FCs (Flowing - F, Ponding - P, and Dry - D) and supported the definition of the hydrotype for the two different river reaches.

The results demonstrate that satellite-based constraints substantially improve the estimation of zero-flow periods, compared to using the hydrological modelling alone. Therefore, the proposed integrated approach effectively combines the strengths of both approaches, allowing hydrological modelling to fill temporal gaps and remote sensing to constrain model-based predictions, ultimately enabling a more reliable daily reconstruction of FCs and hydrotype estimation.

Several studies have highlighted the strong uncertainty associated with estimating low-flow values or zero-flow periods in NPRs (Huxter and Van Meerveld, 2012; Zipper et al., 2021), especially using subjective thresholds (Yu et al., 2024). The combination of different technologies is a crucial step to improve the calibration of reliable and justified thresholds. In this context, remote sensing provides valuable information for defining reliable thresholds. Compared with previous approaches based on a few high-resolution images (e.g., De Girolamo et al., 2022), this study demonstrates how a larger dataset of classified images improves the robustness of hydrological threshold estimation. However, one limitation of the proposed approach is the need to calibrate the T1 and T2 thresholds annually, as this prevents the method from being applied to years for which satellite data are not available.

Despite this limitation, the framework provides valuable insights into the spatial variability of flow permanence along the river network. The comparison of FCs' permanence between the two studied reaches, R1 and R2, showed that P and D phases are longer in R1 than in R2. This difference can be explained by channel morphology, as R1 has a wider active channel, a condition that promotes water infiltration into the riverbed. Furthermore, even in the presence of riparian vegetation, a larger portion of the bed is exposed to solar radiation, which promotes evapotranspiration.

Furthermore, the proposed integrated approach proved especially valuable in evaluating long-term flow intermittency through hydrotype classification, as shown in the ternary plots (Figure 9 and S2). Year-to-year variability in the permanence indices (Mf_h, Mp_h, Md_h) was evident, particularly at R1, where in 2023 the reach shifted into the Ephemeral region, indicating increased drying. This shift is consistent with the drought experienced in the area that year (Matzarakis and Nastos, 2024). This transition underscores the sensitivity of R1 to interannual variability. R2 showed more consistent behavior, remaining within the same hydrotype classification (Intermittent-Fluent) across all monitored years. The spatial variability observed is not detectable by traditional on-field measurements, which provide point data that are insufficient to describe the spatial heterogeneities along NPRs. Our integrated approach is capable of capturing these variations effectively, providing information on the three FCs along the entire NPR.

The comparison between satellite-derived permanence values and those generated through the integration of the hydrological model and S2 data (Fig. 9) further supports the reliability of the approach. For both reaches, the satellite-only and model-augmented classifications fell within the same hydrotype region, with close agreement. Notably, the satellite-only estimates tended to underestimate the permanence of the F phase, likely due to cloud cover during rainy events. These findings confirm the potential of the hybrid approach not only to close observational gaps but also to provide robust, continuous classifications for hydro-ecological assessment and water management planning in NPRs.

Furthermore, the classified PS dataset provided an independent benchmark to assess the robustness of the proposed methodology. The consistently high Overall Accuracy (OA) values (exceeding 0.90, Table 6) obtained for both the S2 classification and the integrated approach indicate a strong agreement with the PS parallel dataset. This level of performance implies a limited misclassification rate and, consequently, a constrained error in identifying hydrotypes with S2 alone or with the integrated approach. The estimated error range shown in the ternary plot (Fig. 9) remains fully contained within the corresponding hydrotype region, confirming that potential classification errors do not alter the hydrotype attribution. Overall, these results demonstrate that the methodology is robust and capable of reliably distinguishing F, P, and D conditions across different reaches and years.

In addition, comparing the annual water balance results obtained from the Karst-SWAT model with the zero-flow days derived from the integrated approach provides insight into how evapotranspiration (ET) and deep aquifer recharge regulate flow intermittency. Although approximately 65% of precipitation is lost to ET on average at the island scale (Chartzoulakis et al., 2001; Chartzoulakis and Psarras, 2005), the Keritis Basin exhibits a substantially lower ET contribution during the 2019–2023 period, with interannual variability and peak values of around 40%. In contrast, deep recharge represents a relatively stable component of the water balance, consistently accounting for approximately 30–35% of annual precipitation throughout the study period. Consistent with the complex hydrological behavior of karst systems, these results indicate that deep aquifer recharge plays a dominant role in controlling the annual occurrence of zero-flow days. Conversely, ET primarily modulates the interannual variability and the magnitude of drying events.

Despite the promising results and the novel hydrological insights provided for the region, the satellite data analysis still faces limitations related to channel width and the presence of riparian vegetation within the riverbed, as these factors directly affect the reliability of FC classification from S2 imagery. In the Keritis Basin, S2 data analysis can cover 13.39 km (17.4%) of the river network, corresponding to 44% of reaches with Strahler stream order ≥ 2 and all third-order reaches. Thus, the methodology cannot be extended to the entire river network, but the integration of hydrological modeling and S2 imagery provides valuable information on the frequency and duration of flow intermittency within a significant portion of the entire river network.

Finally, the presented modeling framework has significant policy implications for the management of NPRs. The integrated approach can be scaled up to a regional scale and applied to NPR basins without compulsory field observations by including regionalization studies and hydrological modeling, such as the one presented by Malagò et al. (2016) for the island of Crete, where daily streamflow was simulated across 354 sub-basins. These simulations could be complemented with S2-based classifications to confirm the hydrological simulations and provide hydrotype identification for the rivers in Crete.

6. Conclusions

Addressing the lack of information on the frequency and permanence of Flow Conditions (FCs) in Non-Perennial Rivers (NPRs) is essential for protecting these dynamic environments and their dependent ecosystems. This study presented an integrated methodology that combines S2 imagery with a Karst-SWAT model, applied to two reaches of the Keritis River in Crete, Greece.

The Karst-SWAT hydrological model alone, despite achieving satisfactory performance in simulating streamflow and particularly low-flows, consistently failed to reproduce zero-flow conditions. Simulated discharge in reaches R1 and R2 always remained above zero, even when satellite observations confirmed the absence of flow (i.e., ponding or dry conditions). This limitation underscores the inherent difficulty of representing flow intermittency in complex karst systems using deterministic modelling approaches alone. The proposed framework proves especially effective in such complex hydrogeological settings, where remote sensing data compensate for structural model limitations and enable a more reliable identification of flow intermittency and hydrotype classification.

In total, 699 S2 False-Color Images (FCIs) were classified between March 2019 and December 2023, averaging more than 41 usable images per year per reach. These data were used to estimate annual flow thresholds that mark the transitions from flowing (F) to zero-flow states (T1) and further between ponding (P) and dry (D) conditions (T2). The proposed method enables the estimation of FC permanence in river sections that are sufficiently wide (at least 30 m) and free from dense vegetation canopies. In the Keritis Basin, this represents around 44% of the second-order Strahler reaches within the river network.

Furthermore, the identification of intermittency enables the investigation of the main drivers responsible for these events. The comparison between the Karst-SWAT water balance and zero-flow days obtained from the integrated approach suggests that deep aquifer recharge provides the primary background control on flow intermittency in the Keritis Basin. Interannual peaks in zero-flow days appear to coincide with years when evapotranspiration (ET) exceeds 40% of annual precipitation, indicating a secondary

Table 6
Overall Accuracy and associated errors estimated from confusion matrices analysis, comparing the classification obtained from Sentinel-2 and from the integrated approach with the one obtained using PlanetScope observations (2020–2023).

		Overall Accuracy	Error (%)
R1	Sentinel 2	0.96	3.7
	Integrated approach	0.96	4.6
R2	Sentinel 2	0.95	5.3
	Integrated approach	0.92	8.2

modulatory role of this factor.

This work demonstrates a replicable and robust approach for improving the temporal resolution and accuracy of NPR monitoring, and for providing a valuable tool for hydro-ecological assessments and long-term water resource management in data-scarce Mediterranean basins. The Water Framework Directive (WFD) requires that all regions in Europe prepare water resources management plans and determine the available water resources through hydrological model simulations. Therefore, automated satellite-based classification could enable the determination of NPR flow conditions at the continental scale, supporting regional authorities in managing water resources in terms of quantity, quality, and biodiversity.

Declaration of Generative AI and AI-assisted technologies in the writing process

During the preparation of this work the authors used ChatGPT in order to enhance the clarity and readability of certain sentences. After using this tool/service, the authors reviewed and edited the content as needed and take full responsibility for the content of the published article.

CRediT authorship contribution statement

G. Manfreda: Conceptualization, Investigation, Formal analysis, Methodology, Data curation, Visualization, Writing – original draft, Writing – review & editing. **C. Cavallo**: Conceptualization, Investigation, Methodology, Data curation, Writing – review & editing. **M.A. Lilli:** Resources, Investigation, Formal analysis. **A. Maragkaki:** Resources, Investigation, Formal analysis, Writing – review & editing. **G. Negro**: Investigation, Writing – review & editing. **M.N. Papa**: Conceptualization, Writing – review & editing, Supervision. **N.P. Nikolaidis:** Conceptualization, Supervision, Resources, Writing – review & editing. **P. Vezza**: Supervision, Project administration, Funding acquisition, Investigation, Data curation, Visualization, Writing – original draft, Writing – review & editing.

Declaration of Competing Interest

The authors declare that they have no known competing financial interests or personal relationships that could have appeared to influence the work reported in this paper.

Acknowledgements

This work was supported by the RIVERTEMP project (2022–1-IT02-KA220-HED-000086223), co-funded by the Erasmus+ program of the European Commission. RIVERTEMP focuses on advancing knowledge, training, and collaboration on temporary rivers, aiming to improve their identification, categorization, and sustainable management in the context of climate change and increasing water demand. This research was conducted during the PhD of Giammarco Manfreda, that was also supported by the research project ‘Implementation of Ecological Flows in the Watercourses of the Po River Basin District’ financed by the Po River Basin Authority (Italy). I would like to express my sincere gratitude to Isabelle Brichetto for her valuable feedback and constant support throughout the entire development of this work.

Appendix A. Supporting information

Supplementary data associated with this article can be found in the online version at doi:10.1016/j.ejrh.2026.103431.

Data availability

Data will be made available on request.

References

Abhervé, R., Roques, C., de Dreuzy, J.R., Datry, T., Brunner, P., Longuevergne, L., Aquilina, L., 2024. Improving calibration of groundwater flow models using headwater streamflow intermittence. Hydrol. Process. 38 (6), e15167.

Acuña, V., Datry, T., Marshall, J., Barceló, D., Dahm, C.N., Ginebreda, A., Palmer, M.A., 2014. Why should we care about temporary waterways? Science 343 (6175), 1080–1081.

Allen, D.C., Datry, T., Boersma, K.S., Bogan, M.T., Boulton, A.J., Bruno, D., Zimmer, M., 2020. River ecosystem conceptual models and non-perennial rivers: a critical review. Wiley Interdiscip. Rev. Water 7 (5), e1473.

Allouche, O., Tsoar, A., Kadmon, R., 2006. Assessing the accuracy of species distribution models: prevalence, kappa and the true skill statistic (TSS). J. Appl. Ecol. 43 (6), 1223–1232.

Arnold, J.G., Srinivasan, R., Muttiah, R.S., Williams, J.R., 1998. Large area hydrologic modeling and assessment part I: model development 1. JAWRA J. Am. Water Resour. Assoc. 34 (1), 73–89.

Beck, H.E., Zimmermann, N.E., McVicar, T.R., Vergopolan, N., Berg, A., Wood, E.F., 2018. Present and future Köppen-Geiger climate classification maps at 1-km resolution. Sci. Data 5 (1), 1–12.

Bonada, N., Cañedo-Argüelles, M., Gallart, F., von Schiller, D., Fortuño, P., Latron, J., Cid, N., 2020. Conservation and management of isolated pools in temporary rivers. Water 12 (10), 2870.

Boothroyd, R.J., Williams, R.D., Hoey, T.B., Barrett, B., Prasojo, O.A., 2021. Applications of Google Earth Engine in fluvial geomorphology for detecting river channel change. Wiley Interdiscip. Rev. Water 8 (1), e21496.

Botter, G., Vingiani, F., Senatore, A., Jensen, C., Weiler, M., McGuire, K., Mendicino, G., Durighetto, N., 2021. Hierarchical climate-driven dynamics of the active channel length in temporary streams. Sci. Rep. 11 (1), 1–13.

Breiman, Leo, Jerome, H.Friedman, Richard, A.Olshen, Charles, J.Stone, 1984. Classification And Regression Trees, 1st ed. Routledge.

Carlier, C., Wirth, S.B., Cochand, F., Hunkeler, D., Brunner, P., 2018. Geology controls streamflow dynamics. J. Hydrol. 566, 756–769.

Cavallo, C., Nones, M., Papa, M.N., Gargiulo, M., Ruello, G., 2021b. Monitoring the morphological evolution of a reach of the Italian Po River using multispectral satellite imagery and stage data. Geocarto Int. 37 (25), 8579–8601.

Cavallo, C., Papa, M.N., Gargiulo, M., Palau-Salvador, G., Vezza, P., Ruello, G., 2021a. Continuous monitoring of the flooding dynamics in the Albufera Wetland (Spain) by Landsat-8 and Sentinel-2 datasets. Remote Sens. 13 (17), 3525.

Cavallo, C., Papa, M.N., Negro, G., Gargiulo, M., Ruello, G., Vezza, P., 2022. Exploiting Sentinel-2 dataset to assess flow intermittency in non-perennial rivers. Sci. Rep. 12 (1), 21756.

Cavallo, C., Sarno, L., Papa, M.N., Negro, G., Vezza, P., Ruello, G., Gargiulo, M., 2025. Estimating dry bed periods in non-perennial rivers using S2 satellite data. J. Hydrol., 133416

Chartzoulakis, K.S., Psarras, G., 2005. Global change effects on cropphotosynthesis and production in Mediterranean: the case of Crete, Greece. Agric. Ecosyst. Environ. 106, 147–157.

Chartzoulakis, K.S., Paranychianakis, N.V., Angelakis, A.N., 2001. Water resources management in the island of Crete, Greece, with emphasis on the agricultural use. Water Policy 3, 193–205.

Chawla, N.V., Bowyer, K.W., Hall, L.O., Kegelmeyer, W.P., 2002. SMOTE: synthetic minority over-sampling technique. J. Artif. Intell. Res. 16, 321–357.

Costigan, K.H., Jaeger, K.L., Goss, C.W., Fritz, K.M., Goebel, P.C., 2016. Understanding controls on flow permanence in intermittent rivers to aid ecological research: Integrating meteorology, geology and land cover. Ecohydrology 9 (7), 1141–1153.

Costigan, K.H., Kennard, M.J., Leigh, C., Sauquet, E., Datry, T., Boulton, A.J., 2017. Flow regimes in intermittent rivers and ephemeral streams. Intermittent Rivers and Ephemeral Streams. Academic Press, pp. 51–78.

Cottet, M., Robert, A., Tronchère-Cottet, H., Datry, T., 2023. "It's dry, it has fewer charms!": Do perceptions and values of intermittent rivers interact with their management? Environ. Sci. & Policy 139, 139–148.

Datry, T., Boulton, A.J., Bonada, N., Fritz, K., Leigh, C., Sauquet, E., Dahm, C.N., 2018. Flow intermittence and ecosystem services in rivers of the Anthropocene. J. Appl. Ecol. 55 (1), 353–364.

Datry, T., Truchy, A., Olden, J.D., Busch, M.H., Stubbington, R., Dodds, W.K., Allen, D., 2023b. Causes, responses, and implications of anthropogenic versus natural flow intermittence in river networks. BioScience 73 (1), 9–22.

Datry, T., Boulton, A.J., Fritz, K., Stubbington, R., Cid, N., Crabot, J., Tockner, K., 2023a. Non-perennial segments in river networks. Nat. Rev. Earth & Environ. 4 (12), 815–830.

De Girolamo, A.M., Lo Porto, A., Pappagallo, G., Tzoraki, O., Gallart, F., 2015. The hydrological status concept: application at a temporary river (Candelaro, Italy). River Res. Appl. 31 (7), 892–903.

De Girolamo, A.M., Barca, E., Pappagallo, G., Porto, A.L., 2017. Simulating ecologically relevant hydrological indicators in a temporary river system. Agric. Water Manag. 180, 194–204.

De Girolamo, A.M., Drouiche, A., Ricci, G.F., Parete, G., Gentile, F., Debieche, T.H., 2022. Characterising flow regimes in a semi-arid region with limited data availability: the Nil Wadi case study (Algeria). J. Hydrol. Reg. Stud. 41, 101062.

Dehghani, A.A., Movahedi, N., Ghorbani, K., Eslamian, S., 2023. Decision tree algorithms. Handbook of hydroinformatics. Elsevier, pp. 171–187.

Devia, G.K., Ganasri, B.P., Dwarakish, G.S., 2015. A review on hydrological models. Aquat. Procedia 4, 1001–1007.

Dohman, J.M., Godsey, S.E., Hale, R.L., 2021. Three-dimensional subsurface flow path controls on flow permanence. Water Resour. Res. 57 (10), 1–18.

Döll, P., Schmied, H.M., 2012. How is the impact of climate change on river flow regimes related to the impact on mean annual runoff? A global-scale analysis. Environ. Res. Lett. 7 (1), 014037.

Eini, M.R., Javadi, S., Delavar, M., Gassman, P.W., Jarihani, B., 2020. Development of alternative SWAT-based models for simulating water budget components and streamflow for a karstic-influenced watershed. Catena 195, 104801.

EU, 2000, 2000. Directive 2000/60/EC of the European Parliament and of the Council of 23 October 2000 Establishing a Framework for Community Action in. Field Water Policy J. L 327, 1–73.

Francesconi, W., Srinivasan, R., Pérez-Miñana, E., Willcock, S.P., Quintero, M., 2016. Using the Soil and Water Assessment Tool (SWAT) to model ecosystem services: A systematic review. J. Hydrol. 535, 625–636.

Frazier, A.E., Hemingway, B.L., 2021. A technical review of planet smallsat data: Practical considerations for processing and using planetscope imagery. Remote Sens. 13 (19), 3930.

Gakii, C., & Jepkoech, J. (2019). A classification model for water quality analysis using decision tree.

Galelli, S., Castelletti, A., 2013. Tree-based iterative input variable selection for hydrological modeling. Water Resour. Res. 49 (7), 4295–4310.

Gallart, F., Prat, N., García-Roger, E.M., Latron, J., Rieradevall, M., Llorens, P., Froebrich, J., 2012. A novel approach to analysing the regimes of temporary streams in relation to their controls on the composition and structure of aquatic biota. Hydrol. Earth Syst. Sci. 16 (9), 3165–3182.

Gallart, F., Cid, N., Latron, J., Llorens, P., Bonada, N., Jeuffroy, J., Prat, N., 2017. TREHS: An open-access software tool for investigating and evaluating temporary river regimes as a first step for their ecological status assessment. Sci. Total Environ. 607, 519–540.

Gao, S., Chen, M., Li, Z., Cook, S., Allen, D., Neeson, T., Hong, Y., 2021. Mapping dynamic non-perennial stream networks using high-resolution distributed hydrologic simulation: A case study in the upper blue river basin. J. Hydrol. 600, 126522.

Garreta, R., Moncecchi, G., 2013. Learning scikit-learn: machine learning in python (Vol. 2013). Packt Publishing, Birmingham.

Gilvear, D., Bryant, R., 2016. Analysis of remotely sensed data for fluvial geomorphology and river science. Tools Fluv. Geomorphol. 103–132.

Gómez-Gener, L., Siebers, A.R., Arce, M.I., Arnon, S., Bernal, S., Bolpagni, R., Zoppini, A., 2021. Towards an improved understanding of biogeochemical processes across surface-groundwater interactions in intermittent rivers and ephemeral streams. Earth-Sci. Rev. 220, 103724.

Gupta, H.V., Sorooshian, S., Yapo, P.O., 1999. Status of automatic calibration for hydrologic models: Comparison with multilevel expert calibration. J. Hydrol. Eng. 4 (2), 135–143.
Heiskanen, A.S., Van de Bund, W., Cardoso, A.C., Nõges, P., 2004. Towards good ecological status of surface waters in Europe-interpretation and harmonisation of the concept. Water Sci. Technol. 49 (7), 169–177.
Huxter, E.H., Van Meerveld, H.J., 2012. Intermittent and perennial streamflow regime characteristics in the Okanagan. Can. Water Resour. J. /Rev. Can. Des. Ressour. Hydr. 37 (4), 391–414.
Jaeger, K.L., Olden, J.D., Pelland, N.A., 2014. Climate change poised to threaten hydrologic connectivity and endemic fishes in dryland streams. Proc. Natl. Acad. Sci. 111 (38), 13894–13899.
Jaloree, S., Rajput, A., Gour, S., 2014. Decision tree approach to build a model for water quality. Bin. J. Data Min. & Netw. 4 (1), 25–28.
Jiang, H., Feng, M., Zhu, Y., Lu, N., Huang, J., Xiao, T., 2014. An automated method for extracting rivers and lakes from Landsat imagery. Remote Sens. 6 (6), 5067–5089.
Kantharajan, G., Anand, A., Krishnan, P., Singh, R.K., Kumar, K., Kumar Yadav, A., Lal, K.K., 2022. Applications of S2 satellite data for spatio-temporal mapping of deep pools for monitoring the riverine connectivity and assessment of ecological dynamics: a case from Godavari, a tropical river in India (2016–2021). Environ. Monit. Assess. 194 (8), 558.
Kirkby, M.J., Gallart, F., Kjeldsen, T.R., Irvine, B.J., Froebrich, J., Lo Porto, A., De Girolamo, A., 2011. Classifying low flow hydrological regimes at a regional scale. Hydrol. Earth Syst. Sci. 15 (12), 3741–3750.
Kotsiantis, S.B., 2013. Decision trees: a recent overview. Artif. Intell. Rev. 39, 261–283.
Kourgialas, N.N., Karatzas, G.P., Nikolaidis, N.P., 2010. An integrated framework for the hydrologic simulation of a complex geomorphological river basin. J. Hydrol. 381 (3-4), 308–321.
Krabbenhoft, C.A., Allen, G.H., Lin, P., Godsey, S.E., Allen, D.C., Burrows, R.M., Olden, J.D., 2022. Assessing placement bias of the global river gauge network. Nat. Sustain. 5 (7), 586–592.
Krysanova, V., White, M., 2015. Advances in water resources assessment with SWAT—an overview. Hydrol. Sci. J. 60 (5), 771–783.
Lamrini, B., 2020. Contribution to Decision Tree Induction with Python: A Review. IntechOpen.
Levick, L., Hammer, S., Lyon, R., Murray, J., Birtwistle, A., Guertin, P., Goodrich, D., Bledsoe, B., Laituri, M., 2018. An ecohydrological stream type classification of intermittent and ephemeral streams in the southwestern United States. J. Arid Environ. 155 (March), 16–35.
Llanos-Paez, O., Acuña, V., 2022. Analysis of the socio-ecological drivers of the recreational use of temporary streams and rivers. Sci. Total Environ. 807, 150805.
Llanos-Paez, O., Estrada, L., Pastén-Zapata, E., Boithias, L., Jorda-Capdevila, D., Sabater, S., Acuña, V., 2023. Spatial and temporal patterns of flow intermittency in a Mediterranean basin using the SWAT+ model. Hydrol. Sci. J. 68 (2), 276–289.
Magand, C., Alves, M.H., Calleja, E., Datry, T., Dörflinger, G., England, J., … & Von Schiller, D. (2020). Intermittent rivers and ephemeral streams: what water managers need to know.
Malagò, A., Efstathiou, D., Bouraoui, F., Nikolaidis, N.P., Franchini, M., Bidoglio, G., Kritsotakis, M., 2016. Regional scale hydrologic modeling of a karst-dominant geomorphology: The case study of the Island of Crete. J. Hydrol. 540, 64–81.
Matzarakis, A., Nastos, P., 2024. Greece 2023: Crazy Summer or New Normal—Lessons Not Learned. Atmosphere 15 (10), 1241.
McDonough, O.T., Hosen, J.D., Palmer, M.A., 2011. Temporary streams: The hydrology, geography, and ecology of non-perennially flowing waters. River Ecosyst. Dyn. Manag. Conserv. 259–290.
Messager, M.L., Lehner, B., Cockburn, C., Lamouroux, N., Pella, H., Snelder, T., Datry, T., 2021. Global prevalence of non-perennial rivers and streams. Nature 594 (7863), 391–397.
Mimeau, L., Künne, A., Branger, F., Kralisch, S., Devers, A., Vidal, J.P., 2024. Flow intermittence prediction using a hybrid hydrological modelling approach: influence of observed intermittence data on the training of a random forest model. Hydrol. Earth Syst. Sci. 28 (4), 851–871.
Mohammed, R., Rawashdeh, J., Abdullah, M., 2020. Machine learning with oversampling and undersampling techniques: overview study and experimental results (April). 2020 11th international conference on information and communication systems (ICICS). IEEE, pp. 243–248 (April).
Moriasi, D.N., Arnold, J.G., Van Liew, M.W., Bingner, R.L., Harmel, R.D., Veith, T.L., 2007. Model evaluation guidelines for systematic quantification of accuracy in watershed simulations. Trans. ASABE 50 (3), 885–900.
Munné, A., Bonada, N., Cid, N., Gallart, F., Solà, C., Bardina, M., Prat, N., 2021. A proposal to classify and assess ecological status in Mediterranean temporary rivers: Research insights to solve management needs. Water 13 (6), 767.
Nachtergaele, F.O., Van Velthuizen, H., Verelst, L., Batjes, N.H., Dijkshoorn, J.A., Van Engelen, V.W.P., Shi, X., 2008. Harmonized world soil database (version 1.0). FAO.
Nash, J.E., Sutcliffe, J.V., 1970. River flow forecasting through conceptual models. Part 1: A discussion of principles. J. Hydrol. 10 (3), 282–290.
Neitsch, S., Arnold, J., Kiniry, J., Williams, J., 2011. Soil & water assessment tool theoretical documentation version 2009. Tex. Water Resour. Inst. *1–647*.
Nerantzaki, S.D., Hristopulos, D.T., Nikolaidis, N.P., 2020. Estimation of the uncertainty of hydrologic predictions in a karstic Mediterranean watershed. Sci. Total Environ. 717, 137131.
Nikolaidis, N., Karatzas, G., 2010. Water resources management plan for the Keritis, Therissou and Koiliaris basins.
Nikolaidis, N.P., Bouraoui, F., Bidoglio, G., 2013. Hydrologic and geochemical modeling of a karstic Mediterranean watershed. J. Hydrol. 477, 129–138.
Papafilippaki, A.K., Kotti, M.E., Stavroulakis, G.G., 2008. Seasonal variations in dissolved heavy metals in the Keritis River, Chania, Greece. Global nest. Int. J. 10 (3), 320–325.
Peel, M.C., Finlayson, B.L., McMahon, T.A., 2007. Updated world map of the Köppen-Geiger climate classification. Hydrol. earth Syst. Sci. 11 (5), 1633–1644.
Perleros, C., Vozinakis, K., 2002. Hydrological study of the Chania county, geological map. Organization Development West Crete (ODWC) (Chania, Greece).
Prancevic, J.P., Kirchner, J.W., 2019. Topographic controls on the extension and retraction of flowing streams. Geophys. Res. Lett. 46 (4), 2084–2092.
Pushpalatha, R., Perrin, C., Le Moine, N., Andreassian, V., 2012. A review of efficiency criteria suitable for evaluating low-flow simulations. J. Hydrol. 420, 171–182.
Ricci, G.F., Centanni, M., De Girolamo, A.M., Gentile, F., 2023. Modelling daily streamflow in a temporary karst river system: comparing three approaches using the SWAT model. Hydrol. Sci. J. 68 (3), 462–473.
Rinaldi, M., Gurnell, A.M., Del Tánago, M.G., Bussettini, M., Hendriks, D., 2016. Classification of river morphology and hydrology to support management and restoration. Aquat. Sci. 78, 17–33.
Roy, D.P., Huang, H., Houborg, R., Martins, V.S., 2021. A global analysis of the temporal availability of PlanetScope high spatial resolution multi-spectral imagery. Remote Sens. Environ. 264, 112586.
Sánchez-Gómez, A., Schürz, C., Molina-Navarro, E., Bieger, K., 2024. Groundwater modelling in SWAT+: considerations for a realistic baseflow simulation. Groundw. Sustain. Dev. 26, 101275.
Seaton, D., Dube, T., Mazvimavi, D., 2020. Use of multi-temporal satellite data for monitoring pool surface areas occurring in non-perennial rivers in semi-arid environments of the Western Cape, South Africa. ISPRS J. Photogramm. Remote Sens. 167, 375–384.
Snelder, T.H., Datry, T., Lamouroux, N., Larned, S.T., Sauquet, E., Pella, H., Catalogne, C., 2013. Regionalization of patterns of flow intermittence from gauging station records. Hydrol. Earth Syst. Sci. 17 (7), 2685–2699.
Steiakakis, E., Vavadakis, D., Mourkakou, O., 2023. Groundwater vulnerability and delineation of protection zones in the discharge area of a karstic aquifer—application in Agyia's Karst System (Crete, Greece). Water 15 (2), 231.
Steward, A.L., von, Schiller, D., Tockner, K., Marshall, J.C., Bunn, S.E., 2012. When the river runs dry: human and ecological values of dry riverbeds. Front. Ecol. Environ. 10 (4), 202–209.
Truchy, A., Csabai, Z., Mimeau, L., Künne, A., Pernecker, B., Bertin, W., Datry, T., 2023. Citizen scientists can help advance the science and management of intermittent rivers and ephemeral streams. BioScience 73 (7), 513–521.
Tzoraki, O., Nikolaidis, N.P., 2007. A generalized framework for modeling the hydrologic and biogeochemical response of a Mediterranean temporary river basin. J. Hydrol. 346 (3-4), 112–121.

Van de Bund, W., 2009. Water Framework Directive Intercalibration Technical Report. Part 1: Rivers. Draft. Joint Research Community. Scientific and Technical Reports. Office for Official Publications of the European Communities, Luxembourg, p. 179.

Vidal-Abarca Gutiérrez, M.R., Nicolás-Ruiz, N., Sánchez-Montoya, M.D.M., Suárez Alonso, M.L., 2023. Ecosystem services provided by dry river socio-ecological systems and their drivers of change. Hydrobiologia 850 (12), 2585–2607.

Yu, S., Shanafield, M., Kennard, M.J., 2024. Assessing the Influence of Zero-Flow Threshold Choice for Characterising Intermittent Stream Hydrology. Hydrol. Process. 38 (10), e15300.

Zimmer, M.A., Kaiser, K.E., Blaszczak, J.R., Zipper, S.C., Hammond, J.C., Fritz, K.M., Allen, D.C., 2020. Zero or not? Causes and consequences of zero-flow stream gage readings. Wiley Interdiscip. Rev. Water 7 (3), e1436.

Zimmermann, B., Zimmermann, A., Turner, B.L., Francke, T., Elsenbeer, H., 2014. Connectivity of overland flow by drainage network expansion in a rain forest catchment. Water Resour. Res. 50 (2), 1457–1473.

Zipper, S.C., Hammond, J.C., Shanafield, M., Zimmer, M., Datry, T., Jones, C.N., Allen, D.C., 2021. Pervasive changes in stream intermittency across the United States. Environ. Res. Lett. 16 (8), 084033.